**CaBLAM! A high-contrast bioluminescent $Ca^{2+}$ indicator derived from an engineered *Oplophorus gracilirostris* luciferase**

Gerard G. Lambert[1,*], Emmanuel L. Crespo[2,*], Jeremy Murphy[3], Daniela Boassa[1], Selena Luong[4], Dmitrijs Celinskis[3], Stephanie Venn[2], Junru Hu[5], Brittany Sprecher[1], Maya O. Tree[2], Richard Orcutt[1], Daniel Heydari[1], Aidan B. Bell[4], Albertina Torreblanca-Zanca[1], Ali Hakimi[6], Diane Lipscombe[2], Christopher I. Moore[3], Ute Hochgeschwender[2], and Nathan C. Shaner[1,‡]

[*]*These authors contributed equally to this work.*

[1]Department of Neurosciences, University of California San Diego School of Medicine, La Jolla, CA USA
[2]College of Medicine, Central Michigan University, Mt. Pleasant, MI USA
[3]Carney Institute for Brain Sciences, Department of Neuroscience, Brown University, Providence, RI USA
[4]University of California San Diego, La Jolla, CA USA
[5]National Center for Microscopy and Imaging Research, University of California San Diego, La Jolla, CA USA
[6]Scintillon Institute, San Diego, CA USA

[‡]Correspondence to ncshaner@health.ucsd.edu

**Abstract**

$Ca^{2+}$ plays many critical roles in cell physiology and biochemistry, leading researchers to develop a number of fluorescent small molecule dyes and genetically encodable probes that optically report changes in $Ca^{2+}$ concentrations in living cells. Though such fluorescence-based genetically encoded $Ca^{2+}$ indicators (GECIs) have become a mainstay of modern $Ca^{2+}$ sensing and imaging, bioluminescence-based GECIs—probes that generate light through oxidation of a small-molecule by a luciferase or photoprotein—have several distinct advantages over their fluorescent counterparts. Bioluminescent tags do not photobleach, do not suffer from nonspecific autofluorescent background, and do not lead to phototoxicity since they do not require the extremely bright extrinsic excitation light typically required for fluorescence imaging, especially with 2-photon microscopy. Current BL GECIs perform poorly relative to fluorescent GECIs, producing small changes in bioluminescence intensity due to high baseline signal at resting $Ca^{2+}$ concentrations and suboptimal $Ca^{2+}$ affinities. Here, we describe the development of a new bioluminescent GECI, "CaBLAM," which displays a much higher contrast (dynamic range) than previously described bioluminescent GECIs coupled with a $Ca^{2+}$ affinity suitable for capturing physiological changes in cytosolic $Ca^{2+}$ concentration. Derived from a new variant of *Oplophorus gracilirostris* luciferase with superior in vitro properties and a highly favorable scaffold for insertion of sensor domains, CaBLAM allows for single-cell and subcellular resolution imaging of $Ca^{2+}$ dynamics at high frame rates in cultured neurons. CaBLAM marks a significant milestone in the GECI timeline, enabling $Ca^{2+}$ recordings with high spatial and temporal resolution without perturbing cells with intense excitation light.

## Introduction

Genetically encoded $Ca^{2+}$ indicators (GECIs) play a central role in modern biomedical research, with much of our current understanding of systems neuroscience based on $Ca^{2+}$ imaging. GECIs based on FPs have been the subject of intense engineering efforts for decades, leading to continual improvements to the practical properties of this class of biosensor[1–4]. The GCaMP family of GECIs is currently in its eighth revision[5], with improvements in brightness, sensitivity, and response kinetics continuing to be achieved, and new families of FP-based GECIs continue to push the boundaries of performance[6–9]. Bioluminescence (BL)-based GECIs originated with the *A. victoria* photoprotein aequorin[10–12] and, more recently, luciferase-based BL GECIs have been developed by several groups[13–18], but to date none of these BL GECIs have demonstrated imaging performance remotely comparable to highly optimized FP-based GECIs such as the GCaMP series. Specifically, existing BL GECIs, though often bright enough to image at high framerates, display low contrast between resting and active $Ca^{2+}$ concentrations in cells, especially *in vivo,* limiting their use to observing $Ca^{2+}$ dynamics mainly at the population level. This is due mainly to the high baseline BL emission and often suboptimal $Ca^{2+}$ affinity of these indicators.

Here, we describe the development of a variant of *Oplophorus gracilirostris*[19–21] luciferase (OLuc) engineered to provide increased BL emission *in vitro* along with improved folding and performance in protein fusions. The *in vitro* activity improvement of this variant does not correlate with its observed bioluminescent output in cultured cells, suggesting that diffusion of furimazine (Fz) molecules across the plasma membrane may currently limit the

per-molecule light emission achievable with this class of probes. We found that these new variants of OLuc were highly amenable to sensor domain insertion, making them a favorable scaffold for engineering a BL GECI, "CaBLAM," ("Ca$^{2+}$ BioLuminescence Activity Monitor"). We generated CaBLAM variants exhibiting very high contrast and optimized $Ca^{2+}$ affinity useful for imaging $Ca^{2+}$ dynamics in the cytosol of living cells at high frame rates. The directed evolution process for the luciferase focused on maintaining high brightness while improving solubility of fusions. Optimization of the C-terminal peptide sequence was a critical component of both luciferase and GECI engineering and was particularly important for obtaining the high contrast currently unique to CaBLAM.

The luciferase, "SSLuc" ("Sensor Scaffold Luciferase"), is several-fold more active than NanoLuc *in vitro* using Promega's proprietary Fz substrate and is less prone to aggregation than NanoLuc when fused to other proteins, but paradoxically does not appear brighter in mammalian cells. The BL GECI, CaBLAM has similar maximum light output to other described BL GECIs in cells and displays a ~97-fold full-range contrast *in vitro* and up to 15-20-fold in live cultured cells in response to physiological changes in cytosolic $Ca^{2+}$ levels. We further demonstrate that CaBLAM can be effectively imaged at up to 10Hz in cultured primary neurons on a typical widefield microscope and EMCCD camera and can reliably report the $Ca^{2+}$ signal from a field stimulation equivalent to a single action potential. We anticipate that these probes will enable a much wider array of researchers to harness the unique advantages of BL for imaging, sensing, and integrating biological activities.

## Results

### Rational design and directed evolution of high-activity soluble OLuc variants

We initially set out to develop a variant of OLuc that could efficiently utilize CTZ, reasoning that NanoLuc was only one of the possible endpoints achievable through directed evolution of this lineage of luciferases. Starting from the OLuc mutant eKAZ[22], we performed multiple rounds of directed evolution consisting of alternating error-prone and site-directed mutagenesis libraries in *E. coli*. For each round, variants were selected based on higher bioluminescent emission and solubility. Subsequent engineering of the intact luciferase included the generation of mNeonGreen[23] fusions for enhancement of emission quantum yield, incorporation of a subset of mutations found in NanoLuc[24] and NanoBit[25], optimization of the C-terminal peptide sequence, and fine-tuning interactions between the C-terminal peptide and the rest of the protein. The final clone, which we named SSLuc ("Sensor Scaffold Luciferase", **Fig. 1A**), can be extracted with nearly 100% efficiency from *E. coli* cultures, retains activity *in vitro* over longer storage periods than NanoLuc, and appears to behave more like a monomer in mammalian cells than NanoLuc. Contrary to our original intentions, SSLuc performs best using Fz as its luciferin, though its activity with other CTZ analogs is also higher than we measure for NanoLuc. Interestingly, we found that SSLuc does not appear brighter in mammalian cells than NanoLuc, despite its high performance *in vitro*, suggesting that availability of the luciferin substrate (e.g., Fz) may limit SSLuc's maximum brightness in cells. SSLuc proved to be a favorable luciferase scaffold from which to generate biosensors, and led us to develop a novel high-performance BL GECI, as described below. A detailed account of our development and

characterization of SSLuc can be found in **Supplementary Results and Discussion, Supplementary Table 1, and Supplementary Figures 1-3**.

**Development and evaluation of a high-contrast BL GECI**

We next explored the design of new BL GECI architectures based on SSLuc. Since the related split luciferase NanoBit[25] was specifically developed as a *reversible* complementation system, we chose the loop between the last two beta strands of the luciferase domain of SSLuc as our split point for insertion of sensor domains, with the goal of generating indicators with a large change in BL output between low and high cytosolic $Ca^{2+}$ concentrations (i.e. [$Ca^{2+}$] between ~100nM and ~1μM). We trialed several topologies for the sensor, including circularly permuted variants and simple sensor domain insertions of RS20-Calmodulin (RS20-CaM), CaM-RS20, and Troponin C (**Supp Fig. 4**). All versions of the initial GECI displayed readily measurable and fairly large changes in BL between $Ca^{2+}$-free and high-$Ca^{2+}$ conditions *in vitro*, with the highest contrast consistently observed from variants with RS20 followed by CaM inserted before the C-terminal luciferase peptide (**Fig 1A, B**). Contemporaneously with our exploration of all these topologies, an analogous RS20-CaM configuration was also identified by Farhana et al[14], in which the insertion is an entire GCaMP sensor domain, including the circularly permuted GFP component. In our designs, the fluorescent protein, if present, remains fixed at the N terminus of the luciferase as a FRET partner to enhance the quantum yield of emission[16,17,26,27], and the $Ca^{2+}$-sensitive signal is restricted to the BL channel, not both channels, unlike GLICO's bimodal signal. Despite this substantial difference and the use of the SSLuc scaffold rather than NanoBit, we found that the tripeptide linker sequences flanking the sensor domains of GLICO were suitable for our new GECI designs as well, and so we adopted these in our final design.

Unexpectedly, the initial clones of our novel BL GECI lineage displayed $Ca^{2+}$ affinities far too high to be practical in living cells, often with $K_D$ < 10nM [$Ca^{2+}$]. We explored several ways of altering the affinity, including the use of alternate RS20 and CaM sequences derived from existing fluorescent GECIs[28–30] and lower-affinity designed variants of the RS20/CaM pair[31], altering the linker length and composition between the RS20 and CaM, altering linker lengths and compositions between the luciferase and sensor domain, and rational directed mutations to the CaM domain's EF-hand motifs. This combination approach allowed us to select for the brightest clones while also determining which design factors influenced the $Ca^{2+}$ affinity. Ultimately, the best balance of brightness, affinity, and Hill coefficient was achieved using the CaM and RS20 sequences from GCaMP6s coupled with a single point mutation (N98I in full-length calmodulin) chosen from among several naturally occurring mutations in human calmodulins leading to heart rhythm defects[32], producing apparent $Ca^{2+}$ binding affinities around 500nM. This $K_D$ target was selected to align the most sensitive part of the GECI's response curve with a physiologically relevant range of $Ca^{2+}$ concentrations—for example, $Ca^{2+}$ concentrations in the cytosol of rat CA1 hippocampal pyramidal neurons in slices have been measured using small molecule dyes[33] and are estimated to range from 32-59nM when resting and up to >300nM in response to a single action potential. The process of evaluating the many variables contributing to the calcium-binding behavior of this BL GECI architecture

generated multiple related BL GECI variants suitable for future optimization and engineering for specific biological use cases requiring higher and lower $Ca^{2+}$ affinities.

To maximize the BL signal contrast between inactive and active cytosolic $Ca^{2+}$ concentrations, we systematically evaluated variants of the C-terminal SSLuc peptide, initially choosing peptides described from the development of NanoBit[25] as we had previously done during SSLuc optimization. We found that the clones displaying the highest contrast in luciferase activity between low and high [$Ca^{2+}$] contained the low-affinity peptide **VTGYRLFEEIL** ("pep114"). We then designed peptides based on this core sequence, drawing inspiration from the best-performing peptides identified during the evolution of SSLuc (**Supp. Table 1**). Ultimately, this led us to choose the peptide **VTGYRLLEEISN** for the final variant, which we named "CaBLAM." The rationale for the design of this peptide, which contains two glutamate residues substituted for the preferred lysines in SSLuc, was to maintain enzymatic activity (largely from the arginine side chain that forms part of the putative active site[34]) while also reducing affinity for the large piece of the luciferase to increase the contrast in luciferase activity between the unbound and $Ca^{2+}$-bound states. We speculate this low affinity allows the C-terminus of the luciferase to disengage from the enzyme more fully under low $Ca^{2+}$ concentrations, decreasing luciferase activity at baseline. *In vitro* characterization of CaBLAM indicated that it has a $K_D$ of ~460nM [$Ca^{2+}$] and an absolute contrast (i.e., the ratio of luminescence emission between saturating $Ca^{2+}$ and zero $Ca^{2+}$, typically reported for this class of sensor) of ~97-fold (**Fig. 1C, Table 1**). This value compares favorably to other published BL GECIs, all of which display substantially lower contrast than CaBLAM[14,17,18]. The Hill coefficient of CaBLAM is ~3, similar to that of GeNL($Ca^{2+}$)_480[17] and notably higher than that of CaMBI[18], which displays a Hill coefficient of ~1.2 in our hands (**Fig. 1C, Table 1**). CaBLAM also has a similar $Ca^{2+}$ affinity to GeNL($Ca^{2+}$)_480, making these two GECIs a well-matched pair for benchmarking in cells. In practice, when a GECI is expressed in a living system, its contrast drops dramatically compared to *in vitro* values, and so we next evaluated the behavior of CaBLAM in cultured cells in comparison with the published GeNL($Ca^{2+}$)_480 GECI.

**Characterization and evaluation of CaBLAM in cells**

We first evaluated CaBLAM variants by widefield imaging of U2OS (human osteosarcoma) cells, which display only small spontaneous changes in cytosolic $Ca^{2+}$ concentration in our hands. CaBLAM consistently generated large changes in BL with ionomycin treatment with a dynamic range 5.4±0.1-fold higher (95% confidence interval (95%CI)) than that of GeNL($Ca^{2+}$)_480 (**Fig. 2A**). Coupled with the *in vitro* characterization data, these results suggest that the larger contrast for CaBLAM over GeNL($Ca^{2+}$)_480 in cells is due to the lower baseline luminescence of CaBLAM coupled with its favorable Hill coefficient. The contrast achievable in living cells sets CaBLAM apart from existing BL GECIs, and is expected to enable observation of small changes in $Ca^{2+}$ concentration more readily than is currently possible.

To address some potential shortcomings of ionomycin experiments and observe a physiologically generated $Ca^{2+}$ signal, we next evaluated the performance of CaBLAM in HeLa cells, known to undergo large oscillations in cytosolic $Ca^{2+}$ in response to a number of stimuli[35]. We observed strong asynchronous oscillations in single-cell BL signals over varying time scales in HeLa cells treated with L-histamine. In parallel experiments, we were able

to observe small changes in cells expressing GeNL($Ca^{2+}$)_480, with a dynamic range 3.3±0.1-fold (95%CI) lower than observed with CaBLAM, consistent with the results of previous ionomycin experiments (**Fig. 2B**). CaBLAM revealed a wide variety of $Ca^{2+}$ oscillation phenotypes in these imaging experiments, with periods ranging from seconds to minutes (**Fig. 2D** and **Supp. Movie 1**).

We compared the high-$Ca^{2+}$ brightness (maximal brightness) of CaBLAM compared with GeNL($Ca^{2+}$)_480 by normalizing the signal to the mNeonGreen fluorescence signal for each. However, as with SSLuc, we observed an unexpectedly weak correlation between fluorescence and BL brightness in all but the lowest-expressing cells for both GECIs, which we suspect is due to rate-limiting substrate diffusion across the plasma membrane. Analysis of the cells with low expression of each sensor indicates that CaBLAM is ~39% ± 19% as bright as GeNL($Ca^{2+}$)_480 on a per-molecule basis (95%CI). The uncertainty in this estimate is high due to the weak linear correlation between fluorescence and BL intensity for both indicators, even at low expression levels (**Supp Fig. 5**).

Finally, we evaluated CaBLAM in cultured primary rat cortical neurons to determine whether it was suitable for real-time reporting of depolarization-induced $Ca^{2+}$ influx. Neurons expressing CaBLAM were imaged similarly to the U2OS and HeLa cells in the previous assays, with dark background frames collected followed by injection of Fz diluted in medium, imaging for 60s, then injection of concentrated KCl to give a final extracellular concentration of 30mM KCl. Upon injection of KCl, the neurons were expected to depolarize, opening voltage-gated $Ca^{2+}$ channels and subsequently inducing secondary $Ca^{2+}$ release to the cytosol from the ER. Consistent with previous contrast measurements in cell lines, these neurons generated a ~15-fold increase in BL emission from CaBLAM between resting and depolarized cytosolic $Ca^{2+}$ levels (**Fig 2C**). We performed identical experiments using GeNL($Ca^{2+}$)_480 and observed a 3.8±0.1-fold lower contrast, consistent with ionomycin and histamine experiments in cell lines.

**Comparison of CaBLAM to GCaMP8s in rat hippocampal neurons**

We benchmarked CaBLAM against a current best-of-class fluorescent $Ca^{2+}$ indicator, GCaMP8s[5], in cultured rat hippocampal neurons transduced with AAV vectors for CaBLAM and GCaMP8s. Based on the characterization experiments performed for the GCaMP series of indicators, we imaged at 10Hz, which we found to be currently optimal for CaBLAM imaging in neurons. BL probes are generally thought to be too dim to image at such high speeds, but we found that we could readily collect quantifiable single-neuron data under these conditions using CaBLAM. Neurons were subjected to field stimulation equivalent to 1, 3, 5, 10, 20, 80, and 160 action potentials (AP). CaBLAM consistently generated BL signals above noise in response to even the 1AP field stimulation when imaged at 10Hz, and spontaneous activity was clearly detectable prior to field stimulation (**Fig 3A, B, Supp. Movie 2**). The median signal to RMS noise ratio (SNR) of neurons responding to 10AP stimulation was ~20 for CaBLAM compared with ~137 for GCaMP8s under identical experimental conditions, consistent with the lower signal intensity of BL emission relative to fluorescence. Some neurons expressing CaBLAM reached a SNR of up to ~50 with 10AP stimulation (e.g., the representative neuron trace shown in **Fig. 3A, B**). The higher contrast of CaBLAM relative to GCaMP8s accounts for at least part of its remarkably reliable performance in detecting

small signals (including spontaneous activity) despite the higher baseline noise (lower absolute intensity). Additionally, we observed substantial photobleaching of GCaMP8s during the ~400s imaging period in this imaging assay, while the CaBLAM baseline signal remained essentially flat throughout (e.g., the single-neuron trace from **Fig. 3A**). In general, CaBLAM and other BL indicators can be imaged continuously for indefinite time periods as long as a fresh supply of luciferin (e.g., Fz) is continuously perfused over the cells.

The response kinetics of CaBLAM are considerably slower than GCaMP8s, as expected since it has not yet been optimized for fast responses (**Fig 3C**). *Because these experiments did not include synaptic blockers*, the true indicator kinetics are likely faster than measured. We determined the rough half-time to peak after field stimulation to be ~700ms for CaBLAM for 10AP stimulations and the half-decay time of >1s. GCaMP8s[5] was reported to have a half-rise time of 80ms and a half-decay time of 198ms, but displayed values of ~200ms and ~800ms under our imaging conditions, again indicating that the inclusion of synaptic blockers would likely lead to faster measured response kinetics for CaBLAM as well. Thus, while CaBLAM does not yet match the state-of-the-art fluorescent GECIs in terms of kinetics or SNR, it also represents a large step forward in BL GECI performance, analogous to the early versions of GCaMP that ultimately led to today's advanced fluorescent GECI ecosystem.

We conclude that CaBLAM's properties as a BL GECI, particularly its high absolute contrast and its practical contrast within a physiologically relevant range of $Ca^{2+}$ concentrations, are uniquely well suited to single-cell resolution imaging and other advanced downstream applications.

## Discussion

While the first known GECIs were naturally-occurring bioluminescent proteins[10–12], fluorescent small molecule dyes and FP-based GECIs are the currently most commonly used tools for reporting $Ca^{2+}$ activity in living systems. The primary limitation of bioluminescent probes relative to fluorescent probes has been their lower rate of photons emitted per indicator molecule at saturating $Ca^{2+}$ concentrations. This peak emission intensity can be increased linearly over several orders of magnitude for fluorescent probes simply by increasing the intensity of the excitation light that is delivered to the sample, but is limited by enzyme kinetics in bioluminescent probes. At the same time, all fluorescent probes undergo photobleaching during imaging which worsens as excitation intensity increases. In intact tissues, autofluorescence from endogenous molecules limits detection of weak fluorescent signals, supplying excitation photons becomes a major technical challenge, and confounding effects such as heating from intense excitation are of major concern. Bioluminescent probes hold promise for circumventing these and other limitations of fluorescence, especially when used in deeper tissues.

While the signal-to-noise ratio advantage afforded by elimination of autofluorescent background partially compensates for the low light output of luciferases in imaging, required exposure times have historically been in the tens of seconds, far from what is necessary to observe meaningful $Ca^{2+}$ dynamics and other fast cellular processess. Imaging changes in intracellular $Ca^{2+}$ at high speeds is possible only when the contrast of an indicator is well above the electronic noise in the camera. BL GECIs derived from GeNL imaged at up to 60 Hz in iPS-

derived cardiomyocytes[17], which display very large changes in cytosolic $Ca^{2+}$ concentration relative to most cells, displayed a dynamic range of less than 2-fold despite *in vitro* characterization suggesting much higher contrast. We observe that in HeLa cells displaying smaller swings in $Ca^{2+}$ concentration when responding to histamine stimulation, the high baseline luminescence of the GeNL($Ca^{2+}$) sensor family limits the achievable dynamic range (**Fig. 2**). In neurons, CaBLAM reliably reports responses to single action potential stimulation like GCaMP8s when imaged at 10Hz, and can be imaged indefinitely without photobleaching or phototoxicity. Future improvements to CaBLAM's BL brightness are expected to bring it closer to parity with fluorescent GECIs and allow even faster imaging with lower noise.

Biochemical indicators using BL as their output modality hold the promise of enabling less invasive and deeper imaging of these events than is possible with fluorescent sensors. While the spatial resolution achievable using bioluminescence alone is likely to be at the microanatomic level rather than at single-cell resolution, at least initially, higher effective resolution is possible using multi-modal optical imaging approaches. For example, BL sensors with expression genetically targeted to small subsets of cells (e.g., neurons) can be tagged or co-expressed with fluorescent markers to provide anatomical information at subcellular resolution via standard 2-photon imaging, followed by high-speed widefield BL imaging of activity at lower spatial resolution. Recorded activity data from BL imaging can then be mapped onto the high-resolution fluorescence data. Critically, CaBLAM will facilitate this type of imaging because of its low baseline signal, preventing a washout of true signal from scattered out-of-focus emission that is common for both fluorescent and BL GECIs in thick tissues. We also plan to use CaBLAM to drive optogenetic elements such as channelrhodopsins and light-sensitive transcription factors, making them response to changes in intracellular $Ca^{2+}$, building on previous work fusing bioluminescence and optogenetics[36–42].

Here, we demonstrate that structure-guided engineering and directed evolution can generate large improvements in luciferase solubility and toxicity while maintaining high catalytic activity, and that highly active and soluble luciferases can be used to engineer biochemical indicators with large signal changes in cells. The scaffold and design principles we have identified will be useful in the design and optimization of BL sensors for other biochemical activities as well[43]. In the future, development of improved red-emitting FRET acceptors (such as optimized long Stokes-shift fluorescent proteins) and/or engineering of high-activity, red-emitting substrates for SSLuc/CaBLAM will further enhance the deep-tissue imaging potential of these probes. Continued efforts will also focus on further improving the light production rate of this and other classes of luciferase. Looking forward, if $K_m$ values are maintained at ~10μM, a diffusion-limited luciferase (i.e., $k_{cat}/K_m = 10^8\text{-}10^9\ M^{-1}s^{-1}$) should be capable of generating $10^3\text{-}10^4$ photons per second per molecule, which leads us to hope that there is ample room left for future improvements to these enzymes. Given our current observations, efforts to increase the delivery rate of engineered luciferins to the cytoplasm of target cells will be central to realizing the full potential of bioluminescent imaging probes.

## Materials and Methods

### General molecular biology.

*E. coli* strain NEB 10-beta (New England Biolabs) was used for all cloning, library screening, and recombinant protein expression. PCRs were performed using Phusion DNA polymerase (New England Biolabs) and the supplied 'GC buffer' under manufacturer-recommended conditions. DNA oligonucleotide primers were purchased from IDT. Restriction enzymes were purchased from New England Biolabs and restriction digests followed the manufacturer's protocols. All plasmids were constructed using Gibson assembly[44] of PCR or restriction digest derived linear DNA fragments as previously described[23,45]. Unless otherwise noted below, chemicals were purchased from Sigma-Aldrich.

### Construction of *E. coli* expression plasmids and libraries.

All *E. coli* expression plasmids were constructed using the pNCST backbone as previously described[23,45]. A linear DNA fragment of the pNCST vector was generated by PCR (primers, **Supp. Data File 2**). Designed luciferase and novel GECI coding sequences were initially prepared as synthetic genes (IDT), as were many designed variants during directed evolution in cases where site-directed mutagenesis would be impractical. Mammalian expression plasmids encoding GeNL($Ca^{2+}$)_480[17] (plasmid #85205) and CaMBI[18] (plasmid #124094) were obtained from AddGene and amplified by PCR (primers, **Supp. Data File 2**) for insertion into the pNCST expression vector. Error-prone mutagenesis was performed using the GeneMorph II kit (Agilent Technologies) as previously described[23] with a target mutation rate of ~5 base changes per kilobase of amplified product. Site-directed libraries were constructed by Gibson assembly of PCR fragments amplified to introduce mixed-base codons as previously described[23]. Selected clones from library screening were sequenced using standard Sanger sequencing (Eton Biosciences). Libraries were introduced to *E. coli* via electroporation with plating at densities between $10^3$ and $10^5$ colonies per 10cm petri dish of LB/Agar supplemented with 100µg/mL carbenicillin (Fisher BioReagents) and incubated overnight at 37C. All plasmid sequences are provided in the **Supplementary Sequences** text file.

### Luciferin substrates and library screening.

Native coelenterazine (CTZ) was purchased from NanoLight. Furimazine (Fz) stock solution was purchased from Promega as a component of the Nano-Glo® Luciferase Assay System (cat# N1110 or N1120). Because Promega does not disclose the Fz concentration in their stock solution, we hereafter describe Fz concentrations in terms of dilution ratio (typically a 1:500 or 1:1000 dilution of the Fz stock solution for imaging and 1:100 for *in vitro* assays). Error-prone mutagenesis and site-directed libraries of luciferases were screened by spraying a sterile solution of 50µM CTZ or 1:100 Fz in 50mM Tris-HCl pH 7.5 onto individual plates using a small atomizer. For 'manual' screening, the entire screening process was performed in complete darkness or very dim far-red LED light, with care taken to dark-adapt vision prior to starting. Sprayed plates were examined by eye and the brightest colonies were immediately marked. For image-based screening, plates were placed immediately into a light-tight chamber and imaged with a PRIME 95b sCMOS camera (Photometrics), followed by identification of the brightest colonies using ImageJ and manual marking on the plates. Marked colonies were grown individually in 5ml 2xYT medium supplemented with 100µg/mL carbenicillin with shaking at 250 rpm at 37C overnight.

**Protein Expression, Purification, and *in vitro* experiments.**

The pNCST plasmid is useful for protein library screening and expression because it does not require an inducer in most strains of *E. coli*. For characterization of selected luciferase and GECI clones, 1ml of each overnight liquid culture was pelleted by centrifugation and the supernatant was discarded. The bacteria were then resuspended once in ultrapure water to remove residual culture medium and pelleted again by centrifugation, discarding the supernatant. The washed pellet was then resuspended in 400µL B-PER (Thermo) reagent and incubated at room temperature for 20 minutes with gentle rocking to extract soluble proteins, followed by a final centrifugation to pellet insoluble components and yield a clear lysate. Clarified B-PER lysates were used directly for characterization experiments in most cases, since we observed rapid degradation of some proteins when subjected to additional purification procedures. In all cases, proteins prepared as clarified B-PER lysates were assayed within 6 hours of extraction.

For experiments using purified recombinant protein, B-PER lysates were bound to equilibrated cobalt beads as previously described[23,45], washed, and eluted in 50mM Tris-HCl pH 7.5, 150mM NaCl, 500mM imidazole, then buffer-exchanged into 50mM Tris-HCl pH 7.5, 150mM NaCl using Zeba desalting columns (Pierce). Purified proteins were stored at 4C.

For brightness comparisons *in vitro*, B-PER lysates of mNG-fused luciferase clones were diluted in 50mM Tris-HCL pH 7.5, 150mM NaCl to a peak mNG absorbance value <0.05 and 200µL samples were loaded into a clear-bottom black 96 well plate (Corning) along with B-PER lysates from one or more controls (e.g., GeNL). Fluorescence emission spectra were recorded for each sample with excitation at 480nm (5nm bandwidth) using a Tecan M1000Pro Infinite multimode plate reader. To normalize enzyme concentrations based on the fluorescence, a dilution factor was calculated for each well based on the peak fluorescence emission. Samples were then diluted into new wells to a total volume of 50-100µL and were measured again to verify that fluorescence intensities varied by ≤ 5% over all wells. The plate was then transferred to a ClarioStar multimode plate reader (BMG) to measure luminescence kinetics. Luciferin solutions at 50µM (CTZ) or 1:100 (Fz) were prepared in the same Tris buffer as described above and injected in volumes of 100-150µL individually into wells with concurrent measurement of luminescence intensity for a total measurement time of 50s per well. These sample and injection volumes were chosen to reduce variability in measurements due to uneven mixing, which can occur if the injection volume is smaller than the sample volume. Peak and steady-state intensities were then normalized by dividing by the previously measured fluorescence of each well to account for remaining small variations in concentration between wells, and these normalized values were used for brightness comparisons between clones.

For $Ca^{2+}$ titrations *in vitro*, B-PER lysates of mNG-fused GECIs were diluted ~100-fold in 30mM MOPS pH 7.2, 100mM KCl, 10mM $MgCl_2$ and then dispensed into 3 rows (36 wells) of a 96-well plate, 5µL per well. EGTA-buffered $Ca^{2+}$ solutions with free $Ca^{2+}$ concentrations of 2nM, 20nM, 100nM, 200nM, 300nM, 400nM, 600nM, 800nM, 1µM, 1.5µM, 2µM, and 10µM were then prepared from commercial stock solutions (Invitrogen

cat#C3008MP), also in 30mM MOPS pH 7.2, 100mM KCl, supplemented with $MgCl_2$ to a final concentration of 10mM. The presence of Mg2+ is not expected to alter free $Ca^{2+}$ concentrations in EGTA-based buffers and provides a more physiologically relevant environment for this assay. 100µL of $Ca^{2+}$ buffer solution was added to each well containing sample to produce three identical rows of the same concentration series. A solution of 1:100 Fz in the same $Mg^{2+}$-containing MOPS buffer was prepared and injected in volumes of 100µL individually into wells with concurrent measurement of luminescence intensity for a total time of 20s per well. The maximum, steady-state, and area-under-the-curve (AUC) luminescence values were calculated for each well and used to plot the $Ca^{2+}$ binding curve for each GECI. Curve fitting to a sigmoid function was performed using the Solver add-in in Excel to determine the $K_D$, Hill coefficient, and contrast for each GECI tested.

**Construction of mammalian expression plasmids.**

Mammalian expression constructs were mainly generated by Gibson assembly of PCR-amplified coding sequences (primers, **Supp. Data File 2**) into restriction-digested pC1 (CMV promoter, modified from pEGFP-C1, Clontech) or pCAG (CMV enhancer fused to chicken beta-actin promoter) vector fragments. When vector fragment preparation by restriction digest was impractical, we PCR-amplified vector fragments instead (primers, **Supp. Data File 2**). We observed qualitatively less variable and longer-lasting expression using the pCAG vector in most cases. Both vectors were suitable for all constructs tested. Mammalian expression plasmids encoding GeNL($Ca^{2+}$)_480[17] (plasmid #85205) and CaMBI[18] (plasmid #124094) were obtained from AddGene. The plasmid pCAG_EGFP_GPI (plasmid #32601) was obtained from AddGene and digested with *Sac*I and *Xho*I to generate a vector fragment for insertion of GeNL and GeNL_SS for GPI-anchored extracellular display. All plasmid sequences are provided in the **Supplementary Sequences** text file.

**Cell line culture, Transfection, and Imaging.**

HeLa and U2OS cell lines were purchased from ATCC. Cells were maintained under standard culture conditions with incubation at 37C and 5% CO2. Growth medium for HeLa cells was high-glucose DMEM (Gibco) supplemented with 10% fetal bovine serum (FBS) (Gibco), and for U2OS was McCoy's 5a (Gibco) with 10% FBS. For transfection and imaging, cells were plated at a density of 1-2x10^5 cells/ml on coverslip-bottom 35mm dishes (Mattek) or 13mm round coverslips (BioscienceTools) placed in 6-well culture plates and incubated overnight. The following day, cells were transfected using polyethyleneimine (PEI) as previously described[45]. Cells were imaged 24-48h post-transfection.

Prior to imaging non-sensor luciferase constructs and fusions, cells were gently rinsed with fresh medium, leaving 500µL of medium in each dish for Mattek dishes. For cells plated on coverslips, slips were transferred to a low-profile coverslip chamber (BioscienceTools) with a silicone gasket and overlaid with 500µL medium. In either case, cells were transferred to the stage top environmental chamber and allowed to equilibrate for at least 5 minutes prior to imaging.

Image acquisition was performed in a stage-top environmental enclosure (37℃, 5% CO2; Okolab) on a Nikon Ti-E microscope and an Andor iXon Ultra 888 EMCCD camera. Cells expressing bioluminescent constructs

were imaged with a Plan Apo λ 20x Ph2 DM 0.75NA objective (Nikon). For reference fluorescent images in constructs containing mNeonGreen, green fluorescence was excited with a Spectra X LED source (Lumencor) using the 475/28nm channel and a FF495-Di03 dichroic (Semrock) and emission was selected with a FF01-520/35 filter (Semrock). The camera was set to 30MHz EM gain mode with an EM gain setting of 3 for fluorescence acquisition. For bioluminescent signal recording, the illumination source was turned off and emission was collected either with no filter to maximize light collection efficiency or with the FF01-520/35 filter to minimize background light leakage. The camera was set to 30MHz EM gain mode with an EM gain of 300 and exposure times between 50 and 500ms for bioluminescence time series and between 500ms and 10s for single for most datasets.

For $Ca^{2+}$ indicator time series imaging, cells were only plated in Mattek dishes and were not rinsed, a handling method we found prevented induction of extraneous $Ca^{2+}$ signals in the cytosol. Medium was carefully removed to leave 500µL volume remaining in each dish, and 500µL of medium from the dish was reserved and used to dilute the Fz substrate to eliminate small changes in ionic strength and osmolarity that can arise due to evaporation during culture. Baseline images were collected for at least 30s in the dark prior to luciferin addition. Fz diluted in culture medium was added to a final concentration of ~10µM and the BL signal was recorded for 60s. For determination of the maximal contrast in cells, 50µL of concentrated ionomycin was then injected to give a final concentration of 20µM and images were recorded for an additional 60-120s. The concentration of $Ca^{2+}$ in the culture medium was ~1mM (but likely buffered to some degree by other medium components) and therefore expected to produce a "maximal" physiological $Ca^{2+}$ concentration in the cytosol in the presence of ionomycin. For imaging induced $Ca^{2+}$ oscillations, 50µL of concentrated L-histamine was injected to give a final concentration of 50µM and images were recorded for an additional 10-20min.

**Primary Rat Cortical Neuron Culture, Transfection, and $Ca^{2+}$ Imaging.**

Animal procedures were approved by the Institutional Animal Care and Use Committee of UC San Diego. Cortices were dissected out from P2 Sprague-Dawley rats and neurons were dissociated using papain as previously reported[46]. Transfection of neuronal cells with pCAG-CaBLAM and pCAG-GeNL($Ca^{2+}$)_480 was done by electroporation using an Amaxa Nucleofection Device (Lonza) at day-in-vitro 0 (DIV0). Neurons were cultured on poly-D-lysine (PDL) coated 35mm coverslip-bottom dishes (Mattek) in Neurobasal A medium (Life Technologies) supplemented with 1X B27 Supplements (Life Technologies), 2 mM GlutaMAX (Life Technologies), 20 U/mL penicillin, and 50mg/mL streptomycin (Life Technologies) for 2-3 weeks prior to imaging, refreshing half medium every 2-3 days.

For $Ca^{2+}$ imaging with KCl-mediated depolarization, Mattek dishes were treated similarly to cell lines, with removal of all but 500µL medium, equilibration in the stage-top incubation chamber on the microscope, and imaging following the same basic protocol as described above for ionomycin and L-histamine experiments. Dark images were recorded for ~30s, followed by injection of Fz diluted in 1000µL medium at a final concentration of 50µM and incubation for 60s with continuous imaging. Finally, 500µL of 120mM KCl diluted in medium was

rapidly injected to give a final concentration of 30mM KCl, expected to rapidly depolarize all neurons leading to $Ca^{2+}$ influx.

**Primary Rat Hippocampal Neuron Culture, AAV Transduction, and $Ca^{2+}$ imaging.**

Primary E18 rat hippocampal neurons were prepared from tissue shipped from BrainBits (Transnetyx) following the vendor's protocol. Neurons were seeded on PDL-coated 18 mm glass coverslips (Neuvitro) in 12-well tissue culture plates (1 x $10^5$ neurons per well) and grown in Gibco Neurobasal Media supplemented with 2% B27, 0.1% gentamycin and 1% GlutaMAX (all from Invitrogen). The next day, day-in-vitro 1 (DIV1), neurons were transduced with AAV9-Syn (5 x $10^9$ gc per well) encoding jGCaMP8s (AddGene 162374) or CaBLAM (in house prep). AAV9-Syn-CaBLAM was generated by triple lipofection of HEK293-FT cells and harvesting viral particles as previously described[47]. Neurons were imaged between DIV 20 – 30.

For $Ca^{2+}$ imaging with electrical stimulation, cover slips were washed three times and imaged in artificial cerebrospinal fluid, containing (in mM): 121 NaCl, 1.25 $NaH_2PO_4$, 26 $NaHCO_3$, 2.8 KCl, 15 d(+)-glucose, 2 $CaCl_2$, 2 $MgCl_2$ (maintained at ~37 °C, pH 7.3-7.4, continuously bubbled with 95% $O_2$/5% $CO_2$ vol/vol). All imaging was conducted in the RC-49MFSH heated perfusion chamber where the temperature was continuously monitored (Warner Instruments). Only cultures where neurons were evenly distributed across the entire coverslip. In addition, only coverslips with minimal neuronal clumping/astrocytic growth were included for $Ca^{2+}$ imaging. A Teensy 3.2 microcontroller was utilized to synchronize the camera frame number with electrical stimulation using BNC cables connected to EMCCD camera and the SIU-102 stimulation isolation unit (Waner Instruments). Custom written scripts were developed in order to generate analog signals for precise control current stimulation as previously described[48]. Briefly, current field stimulation with a 1ms pulse width at 40mA and 83Hz was utilized. The length of time for each stimulation period was varied (12, 36, 60, 120, 240, 960, 1920ms) in order to achieve the corresponding number of action potentials (1, 3, 5, 10, 20, 80, 160 action potentials).

For fluorescent and bioluminescent $Ca^{2+}$ imaging, a 20x objective lens (0.75 NA) and iXon Ultra 888 EMCCD (Andor Technology) camera were used. Furimazine (Fz) (Promega, N1120) was diluted in bubbled ACSF at concentrations of 1:1000 (0.5x) or 1:500 (1x), both of which provided sufficient bioluminescent signal for imaging at 10Hz. Image acquisition parameters were as follows: 0.09s exposure time, 4.33 us vertical pixel shift, normal vertical clock voltage amplitude, 10MHz at 16-bit horizonal readout rate, 1x pre-amplifier gain, 2x2 binning. The EM Gain was set to 300 for bioluminescent image acquisition and it was not enabled during fluorescent imaging. ACSF was continuously perfused in the heated chamber prior to imaging and during bright field and fluorescence imaging to determine a field of view before beginning bioluminescent $Ca^{2+}$ imaging. During bioluminescent $Ca^{2+}$ imaging, fresh ACSF was utilized to dilute the Fz and kept at 37C in a water bath. Bioluminescent imaging included a 60s initial period of ACSF perfusion without Fz followed with ACSF/Fz at the designated concentration for the remainder of the imaging session. Fz concentration in the imaging chamber typically reached equilibrium within 60s after initiating ACSF/Fz perfusion, as judged by baseline bioluminescent signal in the neuron cell bodies.

**Image processing and data analysis**

All image processing was performed using ImageJ. It is important to note that processing of bioluminescence imaging data requires compensation for the average dark pixel offset arising from the detector's dark current characteristics and by small light leaks in the optical path. For each acquisition setting, dark time series were acquired under identical conditions but without illumination or addition of luciferin substrates. Dark time series with at least 60 frames were used to generate single-frame 'dark' images for each acquisition setting, containing the median value for each pixel over the time series. For single bioluminescence images of fusion proteins, the appropriate dark image was subtracted from the raw image. For time series, the appropriate dark image was subtracted from each frame of the time series. These dark-subtracted time series were summed using the 'Z project' function in ImageJ to create low-noise images for generation of regions of interest (ROIs) for analysis. Additional settings used for image display (e.g., thresholding, output scaling, lookup tables, etc.) are described for individual images in their corresponding figure legends.

To extract data from time series for downstream analysis, ROIs corresponding to individual whole cells were identified from summed time series images using the Cellpose[49] 'cyto' model followed by manual curation. An additional 'background' ROI was drawn manually for each time series in an area devoid of cells. Mean intensities were then measured for each ROI at each time point from the dark-subtracted time series and data transferred to Excel for subsequent steps. The 'background' ROI value was subtracted from each cell ROI at each time point to account for any variable background signal arising from changes in light leakage (for example, when the injection port is uncovered) as well as any bioluminescence generated by extracellular luciferase/GECI molecules that escape from damaged or dead/lysed cells. Note that in cases where cells can be rinsed, the extracellular bioluminescence signal is typically negligible, but baseline shifts from changes in light leakage are inevitable, in our experience, making this step critical for accurate quantitation. For each ROI (whole cell) in a time series, we additionally calculate the mean dark value during the first 30s prior to Fz injection and subtract this value from all time points to bring the dark baseline as close to zero as possible, compensating for any remaining offset in the data not captured by previous processing steps.

For $Ca^{2+}$indicators, the baseline luminescence emission intensity was determined for each cell by taking the average value of time points in the steady-state phase after initial Fz injection but before ionomycin or L-histamine injection, typically observed between 30 and 40s after Fz injection (following a small transient cytosolic [$Ca^{2+}$] increase) in most cells. The indicator signal at each time point was then calculated as the change in luminescence relative to the baseline luminescence ($\Delta L/L_0$) for each cell.

**Acknowledgments**

We wish to thank several individuals who supported this project as allies: Dr. Stephen Adams for many years of insightful discussions about sensors, calcium buffers, and other subjects; Dr. Pauline Wales for her invaluable help with camera and objective selection and optimization; Dr. Justine Allen for critical organizational and administrative support; and Dr. Leona Flores, Dr. Michael Oberholzer, and Dr. David Schoppik for invaluable scientific discussions and moral support through very challenging times. We would also like to thank all members of our Bioluminescence Hub (http://www.bioluminescencehub.org/) laboratories for their feedback, discussions, and thoughtful comments throughout the progression of this work.

**Competing interests**

The authors declare no competing or financial interests.

**Author contributions**

Conceptualization, GGL, ELC, DL, CIM, UH, and NCS; Validation, GGL, ELC, JM, SV, DC, DL, CIM, UH, NCS; Formal Analysis, GGL, ELC, JM, NCS; Investigation, DB, JH, SL, BS, MOT, SV, DC, RO, DH, ABB, ATZ, AH, NCS; Data Curation, GGL, ELC, JM, NCS; Writing—Original Draft, GGL, ELC, NCS; Writing—Review & Editing, GGL, ELC, BS, DL, CIM, UH, NCS; Visualization, GGL, ELC, JM, NCS; Supervision, DL, CIM, UH, NCS; Project Administration, UH, NCS; Funding Acquisition, DL, CIM, UH, NCS

**Data and reagent availability**

Raw and processed data from experiments performed in this study will be made available to other researchers upon request to NCS. Bacterial and mammalian expression plasmids encoding SSLuc, GeNL_SS, and CaBLAM will be deposited for distribution by AddGene (pending); prior to availability from AddGene, plasmids will be shared with non-profit researchers upon request to NCS.

**Funding**

This work was supported by National Institutes of Health grants R21EY030716, R21MH101525, R01GM121944, and U01NS099709, and National Science Foundation grants CBET-1464686 and DBI-1707352.

## Tables

**Table 1.** Properties of selected intensiometric genetically encoded $Ca^{2+}$ indicators

| GECI Name | Type | $K_D$ (nM)[a] | Hill coefficient[b] | Contrast[c] | ref. |
|---|---|---|---|---|---|
| **GCaMP8s** | FP | 46 | 2.2 | 50 | 5 |
| **GCaMP8f** | FP | 334 | 2.1 | 79 | 5 |
| **NEMOf** | FP | 528 | 3.2 | 246 | 6 |
| **NEMOc** | FP | 557 | 3.8 | 422 | 6 |
| **CaMBI_110** | luciferase | 62 ± 16 (110) | 1.2 (2.5) | 4.3 (8) | 18 |
| **GeNL($Ca^{2+}$)_480** | luciferase | 444 ± 150 (480) | 3 (3) | 4.1 (5) | 17 |
| **CaBLAM** | luciferase | 464 ± 115 | 3 | 97 | this work |

[a]Binding constant for $Ca^{2+}$ for FP-based GECIs as reported in the original publications; binding constant for $Ca^{2+}$ as measured *in vitro* for CaMBI, GeNL($Ca^{2+}$)_480, and CaBLAM and (in parentheses) as reported in the original publications. Error margins represent 95% confidence interval for values measured in this work. [b]Hill coefficient (cooperativity) for FP-based GECIs as reported in the original publications; Hill coefficient for luciferase-based GECIs calculated from sigmoidal curve fit to $Ca^{2+}$ titration series and (in parentheses) as reported in the original publications. [c]Contrast between $Ca^{2+}$-free and $Ca^{2+}$-saturated indicator *in vitro* for FP-based GECIs as reported in the original publications; contrast for luciferase-based GECIs measured in this work and (in parentheses) as reported in the original publications.

**Figures**

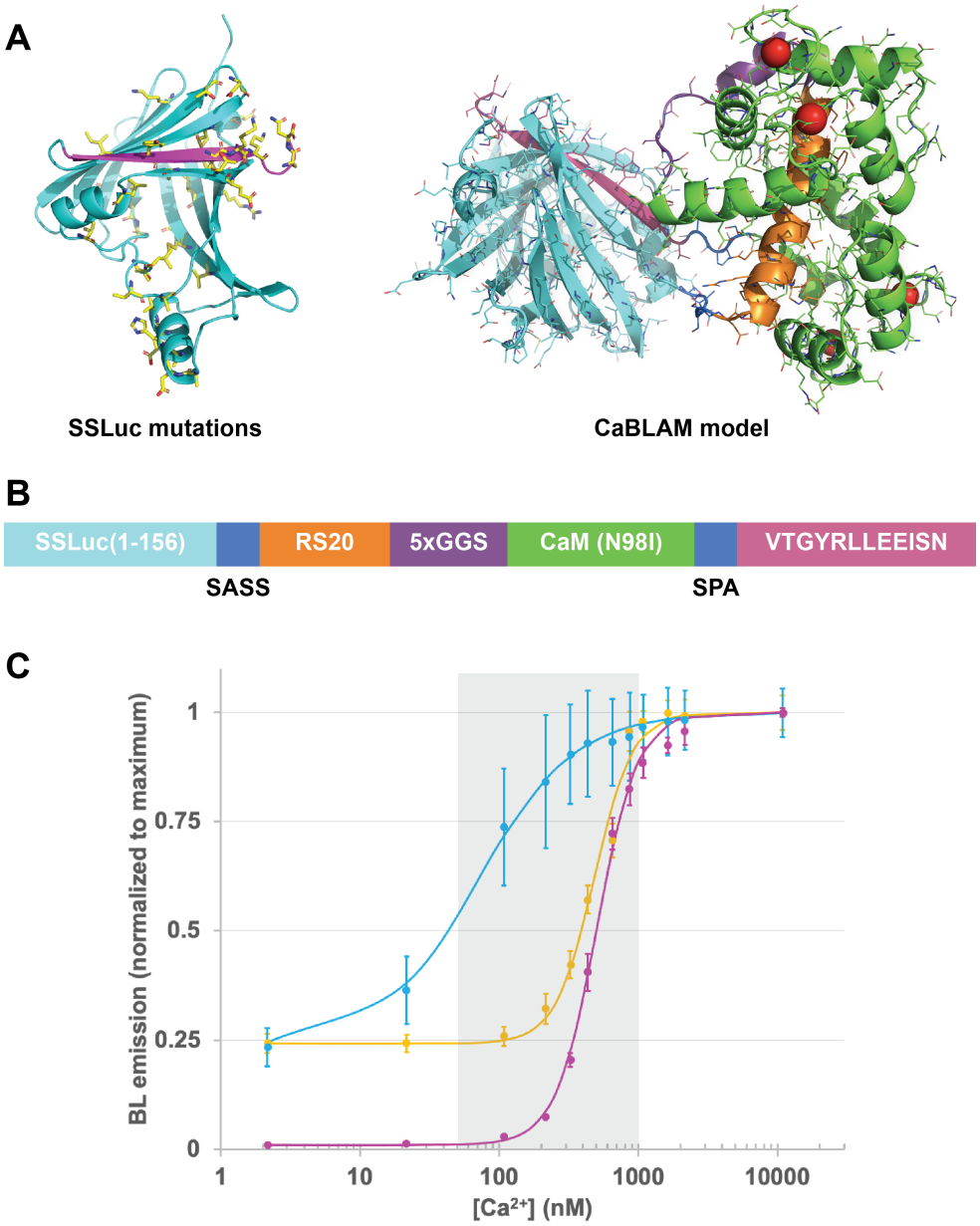


**Figure 1.** CaBLAM architecture and $Ca^{2+}$ affinity. (A) Structure models of eKL9h and CaBLAM. Side chain positions with mutations relative to eKAZ are depicted as yellow sticks in the luciferase model. The C-terminal peptide is depicted in magenta on both structure models. (B) Architecture of CaBLAM (not to scale), with colors corresponding to the model structure backbone. (C) *In vitro* Ca2+ titration of CaBLAM (magenta) alongside GeNL(Ca2+)_480 and CaMBI_110. The physiologically relevant Ca2+ concentration range between 50nM and 1μM is shaded.

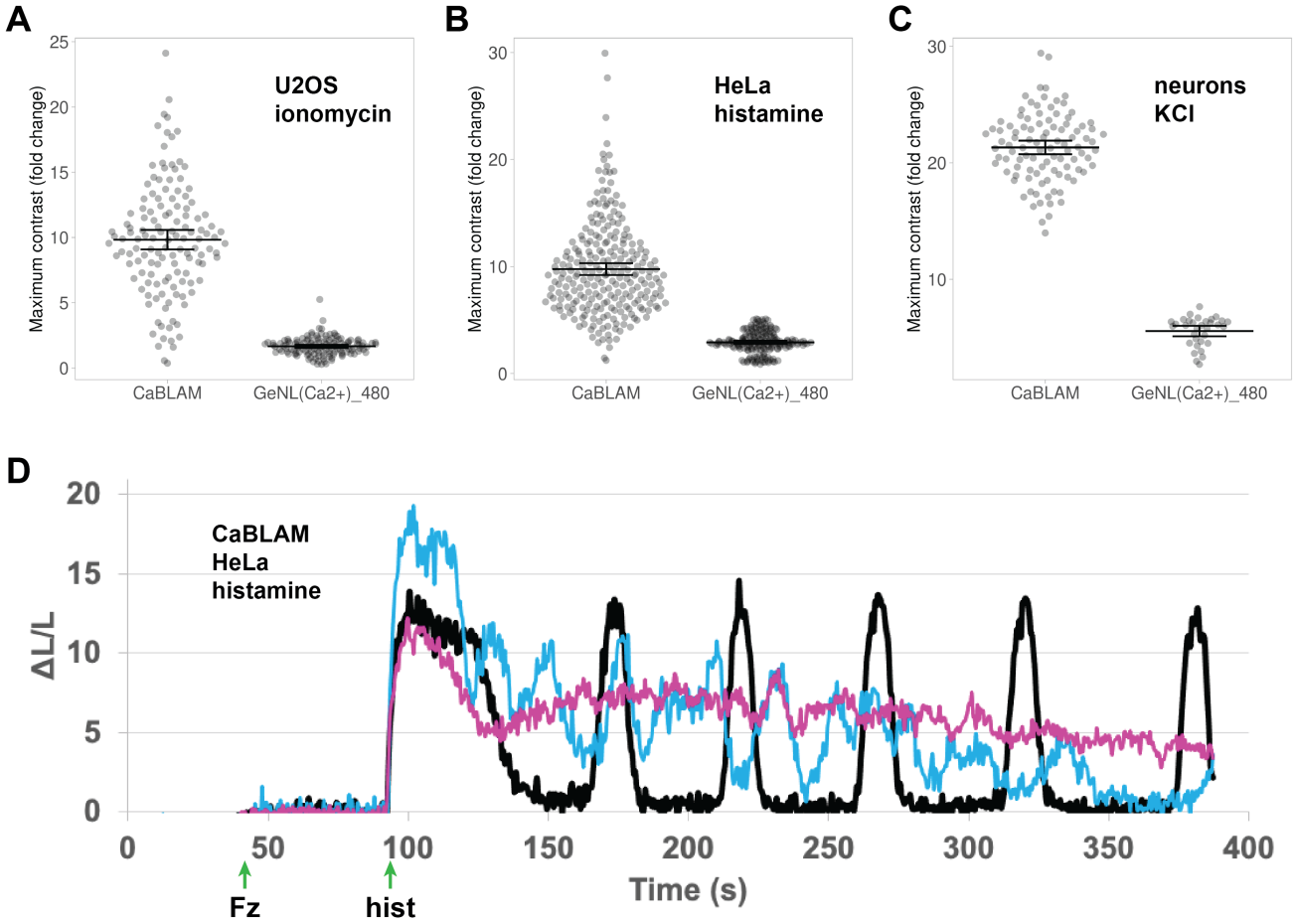


**Figure 2.** Characterization of CaBLAM in cultured cell lines and rat cortical neurons. CaBLAM and GeNL($Ca^{2+}$)_480 in (A) U2OS cells treated with ionomycin and 1mM external $Ca^{2+}$, (B) HeLa cells treated with L-histamine, and (C) rat cortical neurons depolarized with KCl. Data points represent contrast (fold change) between steady-state resting BL GECI signal and peak high-$Ca^{2+}$ GECI signal after treatment. Each point corresponds to a single cell. Mean contrast is shown for each condition with error bars representing the 95%CI for each. (D) Representative CaBLAM signals in HeLa cells treated with L-histamine. Luciferin substrate (Fz) was injected followed ~60s later by concentrated L-histamine, with injection times indicated by green arrows.

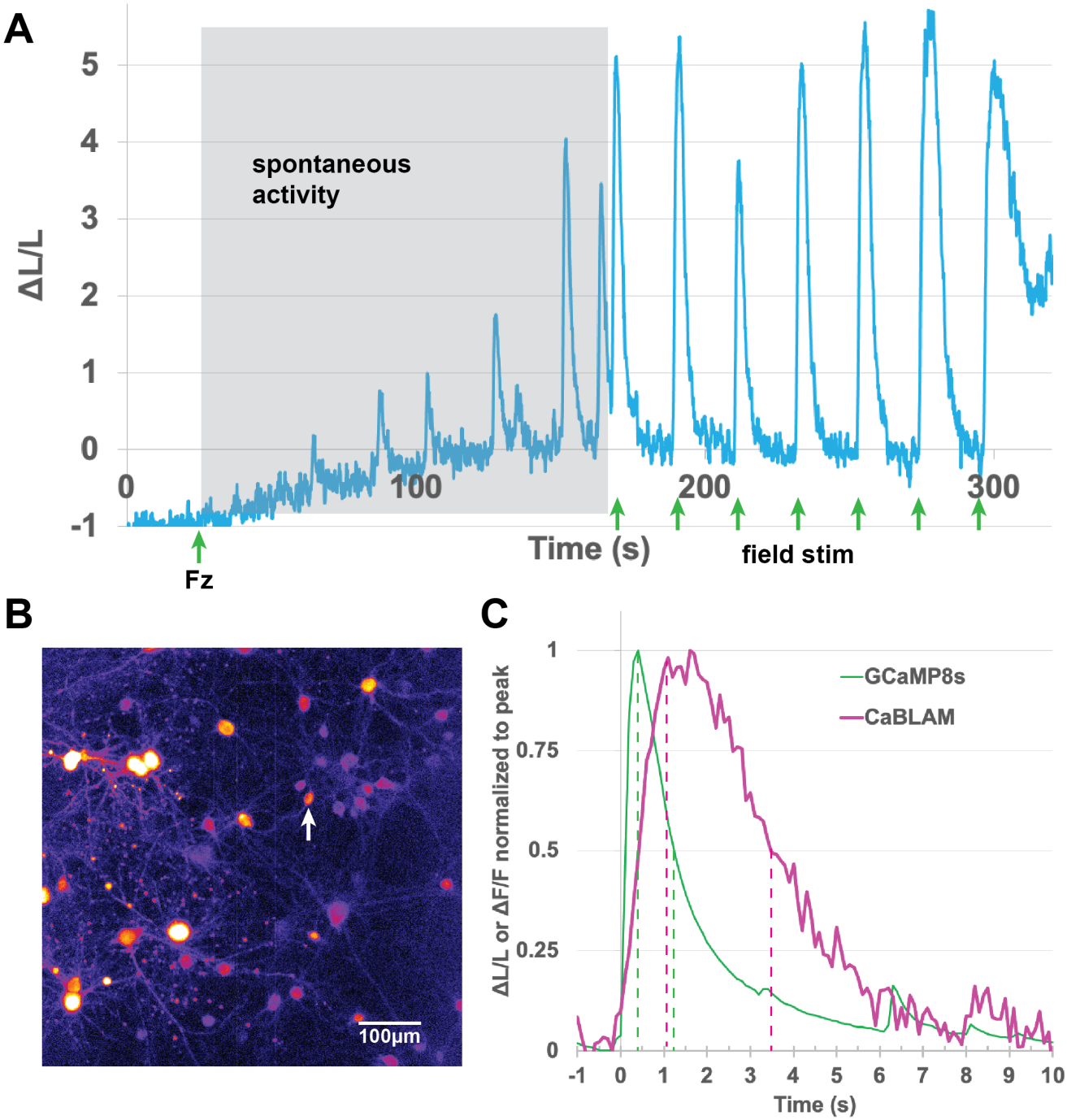


**Figure 3.** CaBLAM performance in cultured rat hippocampal neurons. (A) Representative trace of a single neuron displaying both spontaneous (grey shaded area) and induced $Ca^{2+}$ signals. Luciferin (Fz) was injected where indicated by a green arrow, with a gradual equilibration of baseline luminescence to its steady-state level as spontaneous activity occurs. Field stimulations equivalent to 1, 3, 5, 10, 20 ,80, and 160 action potentials were delivered where indicated by the green arrows. (B) Summed bioluminescence time series from which the data in (A) was derived. The cell shown in (A) is marked with a white arrow. (C) Averaged responses of 13 responsive neurons each for GCaMP8s and CaBLAM imaged with identical treatment illustrating the slower kinetics of CaBLAM relative to GCaMP8s. Peak locations and half-decay points are indicated with dashed lines.

## Supplementary Results and Discussion

### Rational design and directed evolution of high-activity soluble OLuc variants

While NanoLuc displays very high light output utilizing the proprietary furimazine (Fz) substrate, we initially intended to generate a variant derived from *Oplophorus* luciferase that would perform equally well with coelenterazine (CTZ), which is substantially less costly and more readily available. To this end, we started by evaluating the OLuc variant "eKAZ," which was originally described as having higher activity than NanoLuc when utilizing CTZ[22]. We found that the *in* vitro activity of eKAZ appeared highly sensitive to buffer conditions (particularly detergents) and that the activity of purified eKAZ also degraded rapidly upon storage, making it nearly impossible to quantitatively characterize its substrate preference or brightness relative to other luciferases.

To help enhance the luminescence signal of eKAZ by increasing the quantum yield of bioluminescent emission through Förster resonance energy transfer (FRET) to a bright acceptor chromophore[26], we tested several fusions to mNeonGreen[23], using an approach similar to that described by Saito et al. in their design of the original NanoLantern probe[16] (an optimized fusion of the YFP variant mVenus[50] to RLuc8[51]) and later for the GeNL probe[17] (an optimized fusion of mNeonGreen to the N terminus of NanoLuc[24]). We found that a fusion of mNeonGreen to the N terminus of eKAZ, with a 7 amino acid C-terminal deletion to mNeonGreen and proline-proline linker (**Supp. Fig. 1A**), produced a high FRET efficiency (**Supp. Fig. 1B**) and slightly enhanced luminescence intensity compared with eKAZ alone, though at this stage it was difficult to quantify the brightness improvement. We used this construct as the basis for further directed evolution to improve the luminescence activity of this variant, with the expectation that mutations conferring increased CTZ oxidation rates at the expense of luciferase photochemical quantum yield would still display bright luminescence output via FRET coupling.

Because of these clear limitations of eKAZ, we sought to introduce mutations that would improve both its brightness and stability. Following our traditional directed evolution approach, we performed multiple rounds of random and site-directed mutagenesis of the eKAZ variant (fused to mNeonGreen as described above). We screened libraries simply by spraying a sterile solution of CTZ onto agar plates in a dark room and identifying the brightest colonies either by eye or using a homebuilt whole-plate imaging setup. The original clone was already active enough to observe by eye in *E. coli* colonies constitutively expressing the protein from the pNCS expression vector[23]. We immediately identified several key locations in the protein that led to marked increases in colony brightness relative to the original clone. Three mutations (L30Q, S37F, and L92M) were located at an opening to the putative substrate binding pocket[34], one (T13I) was on the first beta strand proximal to the C-terminal peptide, and one (I56T) was internal and possibly part of the binding pocket (numbering based on published NanoLuc crystal structures[34,52]). We targeted positions 56, 92, and 93 in a directed library and identified the mutant L92M/P93E as the most improved clone, designated "eKAZ-L6."

Random mutagenesis of eKAZ-L6 (fused to mNeonGreen as described above) revealed relatively few improved clones, with the mutation A33D present in the brightest variants. We constructed a directed library targeting

position 33 along with previously identified position 30 and positions 68 and 72 on the neighboring alpha helix. We identified the top clone from this library containing the mutations L30V/A33T/F68D/L72H, designated "eKAZ-L9," that displayed both higher luminescence emission and improved soluble protein yield. We suspect that this improvement in solubility arises from substitution of hydrophilic side chains in place of two external hydrophobic side chains (Phe68 and Leu72). At this stage, the *in vitro* activity of eKAZ-L9 had improved substantially compared to the original eKAZ clone[22] and the enzyme had gained a considerably higher tolerance for varied buffer conditions, but still did not display activity levels comparable to NanoLuc using either CTZ or Fz as the substrate.

We reasoned that at this stage of development, merging our improved eKAZ mutations with some mutations from related luciferases such as NanoLuc could be beneficial. Several groups have described the development of split NanoLuc complementation assays and sensors[17,25,53–55]. The most widely adopted bimolecular version, dubbed "NanoBit," was optimized for low affinity between the split pieces to avoid self-complementation[25]. The small fragment ("SmBit") of the NanoBit pair comprises the last beta strand and is only 11 amino acids long. NanoBit was developed by optimizing the large fragment ("LgBit") by directed evolution with selection for the highest BL signal when the C-terminal peptide was added, along with the identification of several functional C-terminal peptides with lower and higher affinities to LgBit (**Supp Table 1**). *We reasoned that the activity- and folding-enhancing mutations present in NanoBit could be useful in improving eKAZ-L9*, and that substitution of the last 11 amino acids with the highest-affinity peptide identified (**VSGWRLFKKIS**, designated as "86" in the NanoBit publication[25]) could further enhance the stability of the folded protein.

In an effort to preserve the substrate specificity of eKAZ-L9 for CTZ, we designed a variant that included only the external NanoBit mutations (several of which are carried over from NanoLuc), reasoning that specificity for Fz was likely to be determined by internal mutations influencing the substrate binding pocket. The resulting designed mutant, designated "eKAZ-11S-L9," contains 22 mutations relative to eKAZ, including the 6 mutations we previously identified through directed evolution, 12 external mutations from NanoBit, and the remaining 4 non-aligned residues arising from substitution of the high-affinity C-terminal peptide "86" in place of the original C terminus. We then tested eKAZ-11S-L9 by constructing a new fusion to mNeonGreen identical in design to GeNL[17], which uses mNeonGreen with a 10 amino acid C-terminal truncation and a Gly-Phe linker before the luciferase with a 5 amino acid N-terminal truncation. We assayed this mutant *in vitro* in parallel with GeNL using *E. coli* extracts, normalizing to the fluorescence intensity (since mNeonGreen is fused to the luciferase, it can act as an internal standard). These experiments revealed that the mNGΔ10C-GF-Δ5NeKAZ-11S-L9 construct was already apparently ~5-fold more active than GeNL on a per-molecule basis using Fz, and ~4-fold using CTZ (data not shown).

At this stage, since activity remained higher with Fz than CTZ even after omitting internal mutations expected to retain preference for CTZ, we reasoned that additional mutations borrowed from NanoLuc might help improve the enzyme further and might additionally enhance activity with both Fz and CTZ. To test this hypothesis, we generated a new variant by introducing most of the internal mutations present in NanoLuc and/or NanoBit that

we had previously excluded in our design: A4E/G15A/Q18L/L27V/K43R/I76V/I90V/P115E/Q124K, in addition to altering the C-terminal peptide to **VSGWRLFEKISN** to bring its sequence midway between that of NanoLuc and NanoBit. The resulting variant was designated "eKL9h" and retained its high activity with CTZ while also displaying increased activity with Fz and other CTZ analogs. When expressed in *E. coli,* the mNG FRET fusion to eKL9h could be fully extracted with B-PER lysis reagent, while GeNL (the equivalent mNG FRET construct with NanoLuc) was largely insoluble (**Supp. Fig. 2**), suggesting that eKL9h might also perform more reliably as a fusion partner to other proteins.

To further increase the brightness of eKL9h, we focused on the C-terminal peptide, individually constructing and characterizing 8 different peptides selected from those characterized during the original development of NanoBit (**Supp. Table 1**). Peptides were chosen to represent the full range of NanoBit affinities, with the expectation that there would be an optimum affinity for activity in an intact OLuc variant. We found that the C-terminal peptide we had originally chosen was already superior to all others tested, though many performed similarly, and we observed no clear correlation between peptide affinity and luciferase activity. While characterizing these C-terminal peptide variants, we serendipitously identified one aberrant clone that displayed approximately 2-fold higher activity than eKL9h. Sequencing revealed that this clone had a frame shift in the C-terminal peptide that led to the unintended sequence **GYRLLKKSCDV**. Based on this sequence, we generated variants with truncations of one to four amino acids from this novel C terminus as well as a set of variants with a GYRLLxK or GYRLxxK leading sequence followed by a variety of rationally designed variations on the trailing sequences (**Supp. Table 1**). We identified the peptide **GYRLLKKISN** as the most optimal of those tested, leading to the luciferase clone eK-ISN.

Based on subtle correlations between sequence and activity in C-terminal peptide variants, we speculated that the lysine side chains at positions 168 and 169 in this new C-terminal peptide might be important for high activity of this lineage of OLuc variants. We explored substitutions to other residues with side chains that could potentially interact with these lysine side chains. We constructed a model of the eKL9h protein structure by homology modeling with a NanoLuc X-ray structure template[52] in Rosetta[56] and identified positions 9, 10, 13, and 146 to target for randomization based on their proximity to the key lysine side chains. We constructed single point mutants for all possible amino acids at these four positions and then measured the luminescence intensity for each clone in comparison with the standards (GeNL and the GeNL-style mNG fusion to eK-ISN) with CTZ, *h*-CTZ, *bis*-CTZ, and Fz substrates. Several substitutions at positions 13 (original residue Thr, replaced by Glu, Ile, His, or Leu) and 146 (original residue Asp, replaced by Glu, Asn, His, or Ser) produced clones with activity equal to or better than that of eK-ISN. We next shuffled these favorable substitutions, producing all possible double mutants. Of these, eK-ISN with the additional mutations T13I and D146E was ~2-fold brighter *in vitro* than eK-ISN, leading to the clone eK-ISN-IE, which we used for subsequent detailed characterization *in vitro* and in mammalian cell lines. Since this clone later proved to be well suited to insertion of sensor domains, we gave this clone the "official" name of Sensor Scaffold Luciferase, or SSLuc.

SSLuc contains 37 amino acid substitutions relative to the active domain from wild-type OLuc, 34 substitutions relative to eKAZ, and 26 substitutions relative to NanoLuc, comprising between 15% and 22% of the total amino acids in this small protein. Peptide sequences of SSLuc, related published OLuc variants, and notable intermediate variants from SSLuc directed evolution are provided in **Supplementary Data File 1**.

Interestingly, Inouye et al[57] recently investigated substrate specificity in NanoLuc, and demonstrated that positions 18 and 27 were important in determining substrate preference, with reversion of these positions to the wild-type residues increasing specific activity with *bis*-CTZ relative to Fz. We did not exhaustively characterize the substrate preference for each mutant generated during the directed evolution of SSLuc in this study, but these intermediate variants may be useful for future studies of structural determinants of substrate preference in this enzyme lineage.

***In vitro* characterization of SSLuc**

We initially compared the properties of NanoLuc and SSLuc using GeNL-style mNeonGreen (mNG) fusions (i.e., mNeonGreenΔ10C-GF-Δ5NSSLuc, hereafter abbreviated to GeNL_SS). The FRET efficiency of SSLuc to mNG in the GeNL_SS construct is slightly lower than that of NanoLuc to mNG in GeNL (**Supp. Fig. 1B**), suggesting that the orientation of the luciferase and FP domains in these two fusions is slightly different. The use of mNG fusions provided an internal fluorescent standard, enabling accurate dilution of the two proteins to equal concentrations for each measurement using either the optical absorbance or the fluorescence emission to measure protein concentration (relative to a purified mNG standard at known concentration). Fusion to mNG is not expected to influence the kinetics or substrate specificity of either luciferase. We found that the substrate specificity of SSLuc was similar to that of NanoLuc, with 20±3-fold higher light output when utilizing native CTZ, 3.8±0.3-fold higher with h-CTZ, 4±1-fold higher with *bis*-CTZ, and 10±1-fold higher output with Fz relative to NanoLuc when measured *in vitro* (**Supp. Fig. 3A**), based on steady-state signals from each enzyme. Both SSLuc and NanoLuc produced large initial intensities that decayed rapidly when using *h*-CTZ as a substrate but did not produce a steady-state signal *in vitro* (**Supp. Fig. 3B**), with SSLuc displaying a larger area under the curve than NanoLuc. These observations suggest that the oxyluciferin produced from *h*-CTZ may be a potent inhibitor of both luciferases and/or that oxidation of *h*-CTZ may lead to covalent inactivation of the active site, as seen by others in *Gaussia* luciferase[58]. In our hands, both CTZ and Fz produced steady-state luminescence at all but the highest GeNL_SS concentrations, with Fz producing only slightly higher peak intensity but longer steady-state ("glow") emission (total light output ~2-fold higher) compared with CTZ (data not shown).

When expressed in *E. coli*, GeNL_SS produced a much higher fraction of soluble protein than GeNL (**Supp Fig. 2**), as measured by the relative mNG fluorescence in the pellet and lysate, suggesting that the folding efficiency and/or solubility of GeNL_SS was superior to GeNL, at least in this expression context. Because mNeonGreen folds robustly in fusion proteins in most cases, total fusion protein concentrations inferred from mNG fluorescence were expected to be accurate, while the active/functional enzyme concentration *could differ substantially if the enzyme itself folds poorly in the fusion*. We suspect this is likely the case with the GeNL fusion (NanoLuc), which could also explain its tendency to form insoluble aggregates in *E. coli.* We additionally found

that recombinant NanoLuc and GeNL typically remain stable for ~12 hours following extraction (with or without further purification) but frequently lose luciferase activity rapidly thereafter, while SSLuc and GeNL_SS appear much more shelf stable. We initially suspected that this effect could be due to oxidation of the single cysteine present in the luciferase but found that addition of DTT or β-ME to purified protein stocks did not prevent loss of activity (data not shown). We now speculate that the GeNL fusion does not maintain a stable fold of the NanoLuc portion of the protein, leading to a slow decay in activity relative to stable mNG fluorescence after extraction from *E. coli,* possibly due to self-aggregation of misfolded NanoLuc domains. By contrast, SSLuc and GeNL_SS retain stable luciferase activity under prolonged storage at 4C, even in clarified *E. coli* lysate without further purification.

As a result of these solubility and stability differences, accurate and repeatable comparative assays of luciferase activity could only be made when proteins were extracted and assayed on the same day; *if the proteins were stored for longer times, we consistently measured an unrealistically high relative brightness of SSLuc/GeNL_SS relative to NanoLuc/GeNL.* Taken together, these observations suggest that differences in solubility and folding between SSLuc and NanoLuc when expressed in *E. coli* are likely responsible for the observed *in vitro* performance improvements in SSLuc, and that the $V_{max}$ of correctly folded SSLuc may in fact still be lower than that of NanoLuc. Unfortunately, the context-dependent folding of NanoLuc greatly limited our ability to quantitatively compare the two enzymes, even in mammalian cells (see below).

### ***In cellulo*** **characterization of SSLuc**

We initially attempted to compare the brightness of NanoLuc and SSLuc in mammalian cells by constructing plasmids for extracellular membrane-bound expression under the rationale that this would most closely replicate *in vitro* assay conditions, especially with respect to substrate availability. Ultimately, we chose to compare cytosolic constructs rather than extracellular ones, as discussed in more detail below. For extracellular targeting, NanoLuc and SSLuc full-length coding sequences alone were directed to the plasma membrane by an N-terminal signal peptide derived from *Gaussia* luciferase followed by the B7 hinge alpha helix[59], fused on the C terminus to mNeonGreen. This construct was expected to place the luciferase on the *extracellular* side of the membrane and the fluorescent protein on the *cytosolic side* of the membrane. We chose this configuration after observing that ***neither*** GeNL or GeNL_SS could be cleanly localized to the membrane when placed entirely on the extracellular side of the B7 hinge sequence or a GPI-anchor sequence (data not shown), suggesting that either the mNeonGreen component or the luciferases may interfere with trafficking.

Cells expressing the extracellular NanoLuc and SSLuc constructs also displayed major differences in localization that prevented us from accurately quantifying brightness differences. While SSLuc localized well to the plasma in this construct, NanoLuc remained trapped in the ER, Golgi, and nuclear envelope without *any* clear localization to the plasma membrane (data not shown). We also observed significantly higher signal with SSLuc versus NanoLuc—far higher than expected from the *in vitro* characterization of the two enzymes (data not shown). We suspect that the reduced solubility of NanoLuc relative to SSLuc and/or the presence of an unpaired external cysteine side chain on NanoLuc leads to misfolding and aggregation that both eliminate luciferase activity and

prevent extracellular display of the enzyme. Because of the substantial differences in trafficking between the NanoLuc and SSLuc proteins in these constructs, we could not quantitatively compare the two enzymes in this assay.

For cytosolic expression, we used the GeNL and GeNL_SS coding sequences driven by a CMV or CAG promoter. We found that the fluorescence brightness of individual cells was generally not correlated linearly to the luminescence brightness for either cytosolic construct, as would be expected in a luciferase-FP fusion construct (data not shown). Our interpretation of this observation is that delivery of the luciferin across the cell membrane is rate-limiting when these luciferases are expressed in cytosol with the substrates we tested (CTZ, *h*-CTZ, *bis*-CTZ, and Fz). We concluded that cytosolic GeNL and GeNL_SS expression was also not a suitable test system for quantitative brightness comparisons in mammalian cells.

Finally, to assay the *in cellulo* brightness of SSLuc versus NanoLuc without the potential complications of using a fusion protein, we finally constructed plasmids to express mNeonGreen and each full-length luciferase separated by a self-cleaving T2A peptide[60] to provide 1:1 stoichiometry of each protein individually. This allowed us to maintain the internal fluorescent standard while measuring the luciferase output independently, which we hypothesized would minimize fusion-dependent misfolding of NanoLuc. Imaging these constructs expressed in U2OS cells revealed that only cells expressing very low levels of recombinant protein displayed an apparently linear relationship between fluorescent and luminescent intensity (data not shown). This observation supports our hypothesis that delivery of luciferin (Fz) across the cell membrane is rate-limiting. Restricting analysis to the linear portion of each curve, we find that SSLuc appears to produce approximately half the photons of NanoLuc when not fused to a FRET acceptor, suggesting that it is indeed "dimmer" on a per-molecule basis when both proteins are properly folded.

**Subcellular imaging of GeNL_SS-tagged proteins**

We fused GeNL_SS to several proteins to evaluate its utility in subcellular localization imaging in living cells. Fusions to H2B, LifeAct, and TOMM20 displayed expected localization in cells for both GeNL and GeNL_SS fusions when expressed at moderate levels (data not shown), but both failed to localize well in the highest-expressing cells. This phenomenon is common to even the most well-behaved fluorescent proteins, and so we note that researchers should *always* be wary of tagged protein localization in the brightest subset of transfected cells. Interestingly, when we compared U2OS cells expressing identical GeNL-H2B and GeNL_SS-H2B fusions, we noticed that the toxicity of the GeNL fusion appeared quite high, with most expressing cells dying within 24h of expression onset, while cells expressing the GeNL_SS fusion remained viable and were able to divide successfully (data not shown). When considered along with its poor localization in extracellular plasma membrane-directed fusions, these observations support the hypothesis (as noted above) that GeNL undergoes a substantial amount of misfolding in mammalian cells just as it does in *E. coli*, especially when targeted to oxidizing compartments, possibly in part because of the unpaired cysteine near its C terminus which is absent in SSLuc/GeNL_SS. It remains possible that NanoLuc alone (without the mNG FRET acceptor) could be a suitable

fusion tag for at least some proteins in mammalian cells, but because we would be unable to easily compare expression levels without the fluorescent component, we chose not to evaluate such fusions in this study.

**Oligomeric state of GeNL and GeNL_SS**

We constructed fusions of GeNL and GeNL_SS to the C terminus of the CytERM peptide used for the OSER assay, a standard assay of "monomeric behavior" for fluorescent proteins expressed in mammalian cells. ***Neither protein*** displayed OSER/NE ratios consistent with currently accepted values for monomeric fluorescent proteins[61] (data not shown), suggesting some amount of self-association. Qualitatively, ER morphology was more evenly labeled in CytERM-GeNL_SS expressing cells compared with CytERM-GeNL, and OSER structures appeared more often in cells with lower expression level (as measured by fluorescence intensity) of CytERM-GeNL compared to CytERM-GeNL_SS, suggesting that GeNL_SS may self-associate to a lesser degree than GeNL. We conclude that while self-association of both GeNL and GeNL_SS appears to be low—neither appears to be a *strong* dimer in this assay—neither probe performs as well as a monomeric fluorescent protein tag for imaging fusion protein localization.

CytERM fusions to NanoLuc and SSLuc alone (without the mNG acceptor) were too dim to obtain images with a signal to noise ratio suitable for quantitative analysis, and as a result we were unable to determine whether the mNG fusions are more or less soluble and monomeric than the untagged luciferases. Additional characterization of the oligomeric state of NanoLuc and SSLuc under physiological conditions will be necessary to clarify the differences between these two luciferases. Taking all data and observations into account, SSLuc appears to have higher solubility, more efficient folding, lower toxicity, and less tendency to self-associate than NanoLuc, but has several areas that would benefit from future engineering to improve catalytic rate, performance as a fusion tag, and overall "inertness" in host cells.

**Supplementary Tables**

**Supplementary Table 1.** C-terminal peptide sequences.

| Peptide name | Sequence |
|---|---|
| eKAZ/Oluc | VTGWRLCENILA |
| NanoLuc | VTGWRLCERILA |
| eKL9h | VTGWRLFEKISN |
| pep101 | VTGYRLFEKES |
| pep104 | VEGYRLFEKIS |
| pep114 | VTGYRLFEEIL |
| pep128 | VTGYRLFEKIL |
| pep79 | VTGYRLFKKISN |
| pep86 | VSGWRLFKKIS |
| pep99 | VTGYRLFEKIS |
| pepNP | VTGWRLFERILA |
| | |
| LKKIS | VTGYRLLKKIS |
| LEKIS | VTGYRLLEKIS |
| LEKISN | VTGYRLLEKISN |
| LEEIS | VTGYRLLEEIS |
| LEKS | VTGYRLLEKS |
| LEKSS | VTGYRLLEKSS |
| LERILA | VTGYRLLERILA |
| CEKISN | VTGYRLCEKISN |
| IKKS | VTGYRLIKKS |
| VKKS | VTGYRLVKKS |
| CKKS | VTGYRLCKKS |
| IEKIS | VTGYRLIEKIS |
| VEKIS | VTGYRLVEKIS |
| KKSCDV | VTGYRLLKKSCDV |
| KKSCD | VTGYRLLKKSCD |
| KKSC | VTGYRLLKKSC |
| KKS | VTGYRLLKKS |
| KK | VTYYRLLKK |
| LKKISN | VTGYRLLKKISN |
| LEEISN | VTGYRLLEEISN |

**Supplementary Figures**

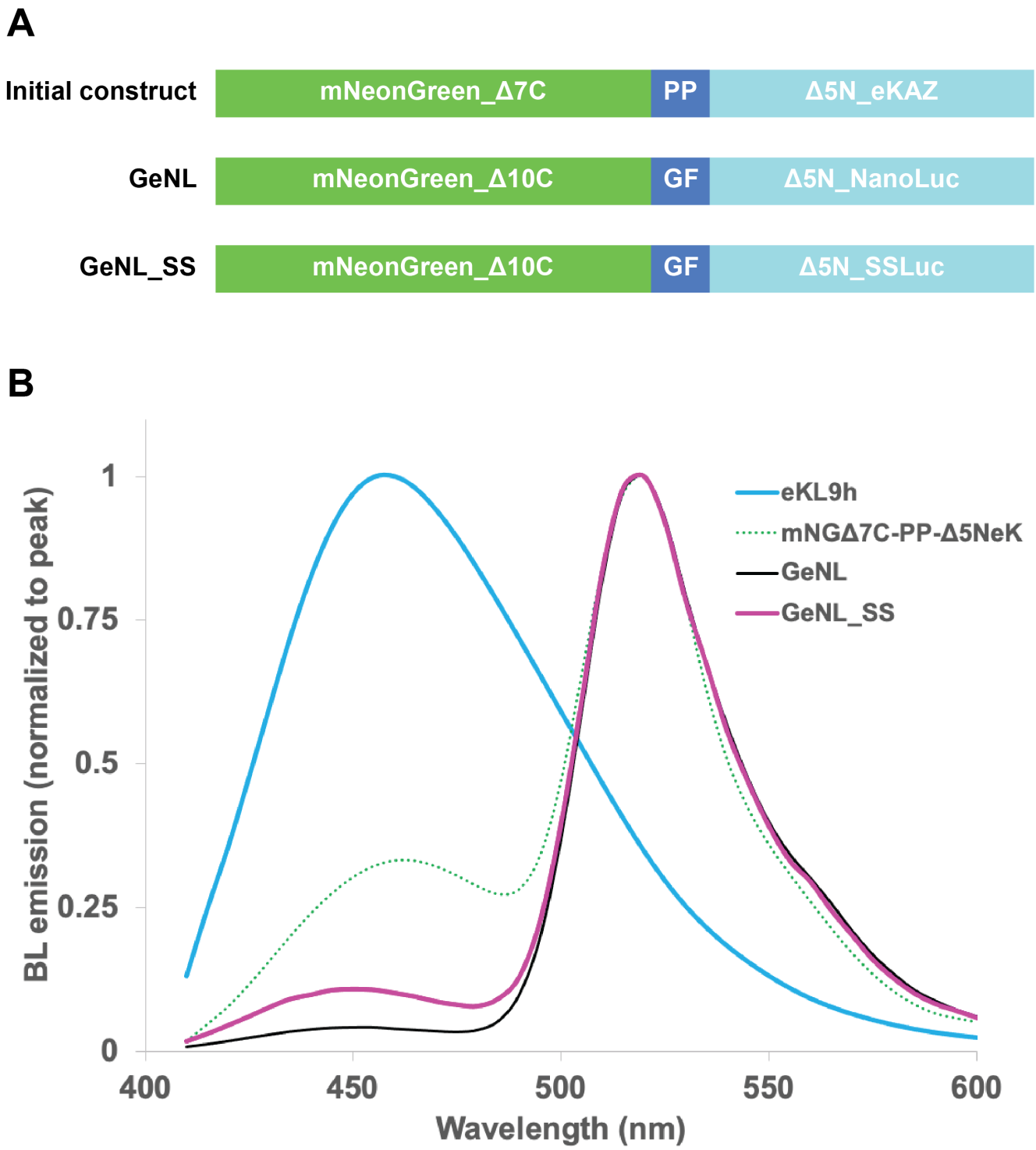


**Supplementary Figure 1.** Constructs and emission spectra. (A) Architecture of the initial mNeonGreen FRET construct with eKAZ, GeNL, and GeNL_SS. (B) Bioluminescence emission spectra for eKL9h (identical to both NanoLuc and SSLuc), initial FRET construct mNGΔ7C-PP-Δ5NeKAZ, GeNL, and GeNL_SS.

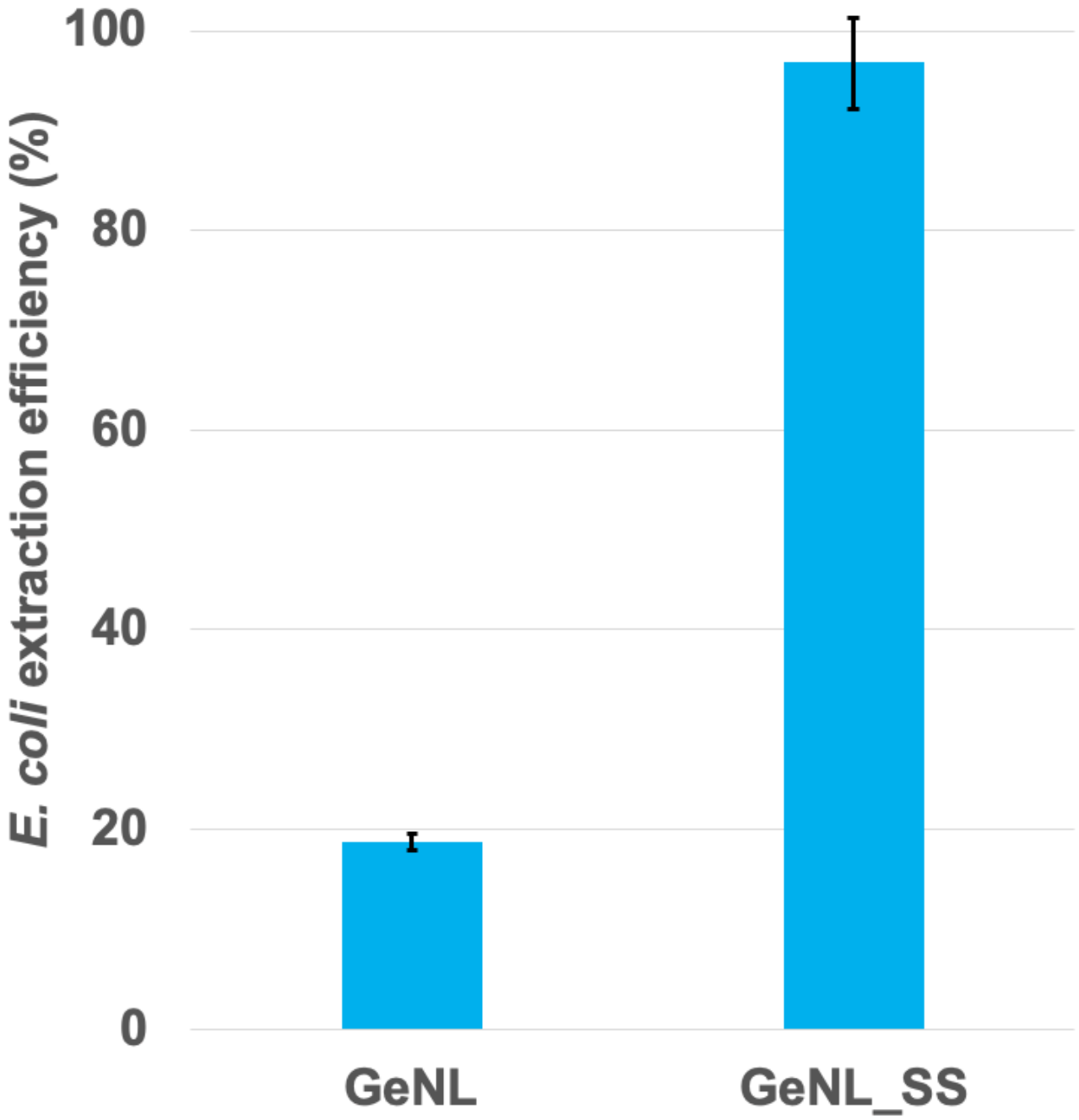


**Supplementary Figure 2.** Extraction efficiency of GeNL and GeNL_SS when expressed from the pNCST vector in *E. coli* and extracted with B-PER reagent. Values shown are the ratio between extracted fluorescence and total pellet fluorescence. Error bars represent 95%CI.

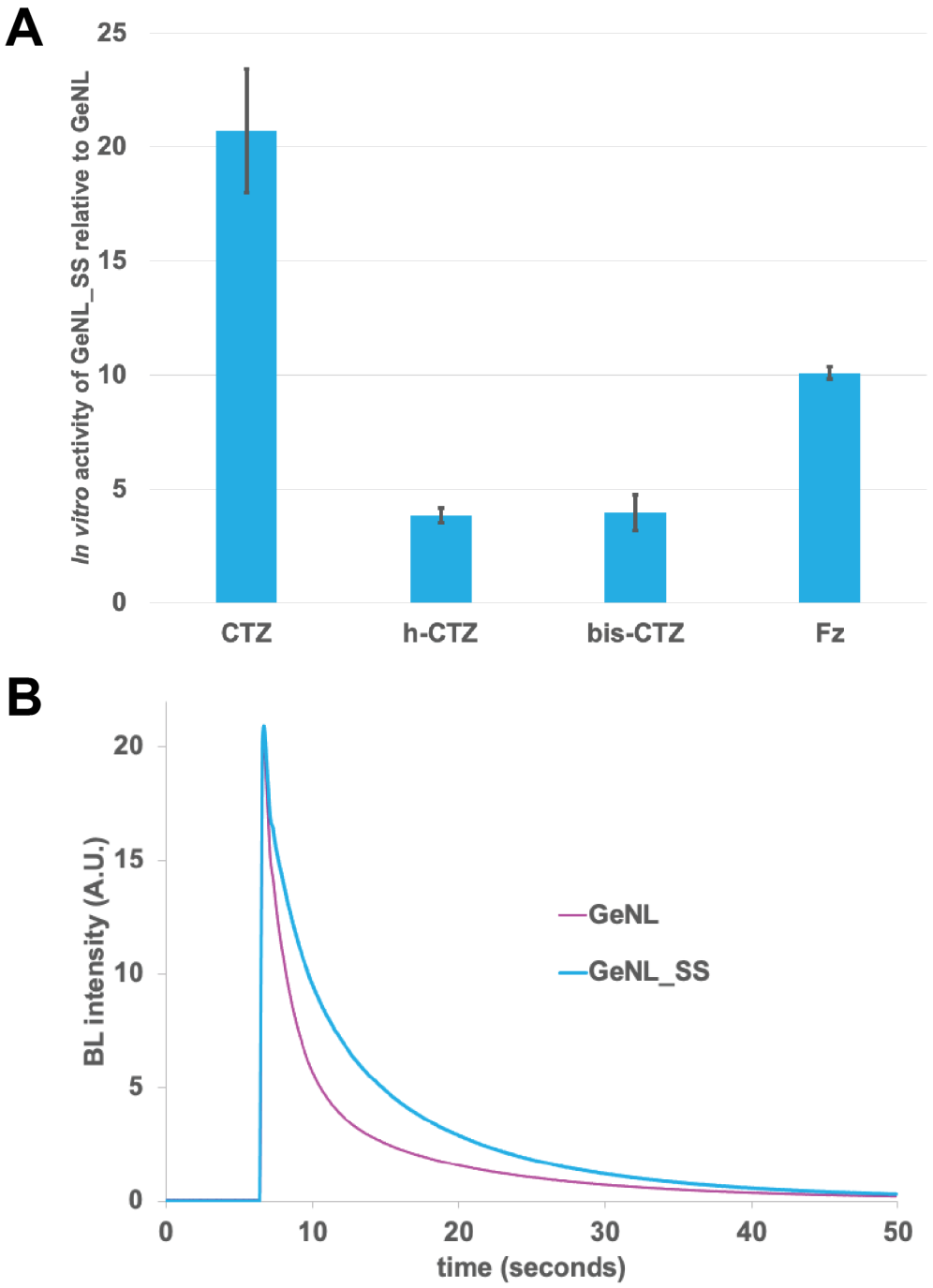


**Supplementary Figure 3.** *In vitro* characterization of SSLuc substrate preference and relative activity. (A) Relative activity with different substrates of GeNL_SS compared to GeNL. Bars represent fold difference of GeNL_SS steady-state intensity relative to equimolar GeNL in *E. coli* expression lysates. Error bars represent 95%CI. (B) Kinetic behavior of GeNL and GeNL_SS with *h*-CTZ.

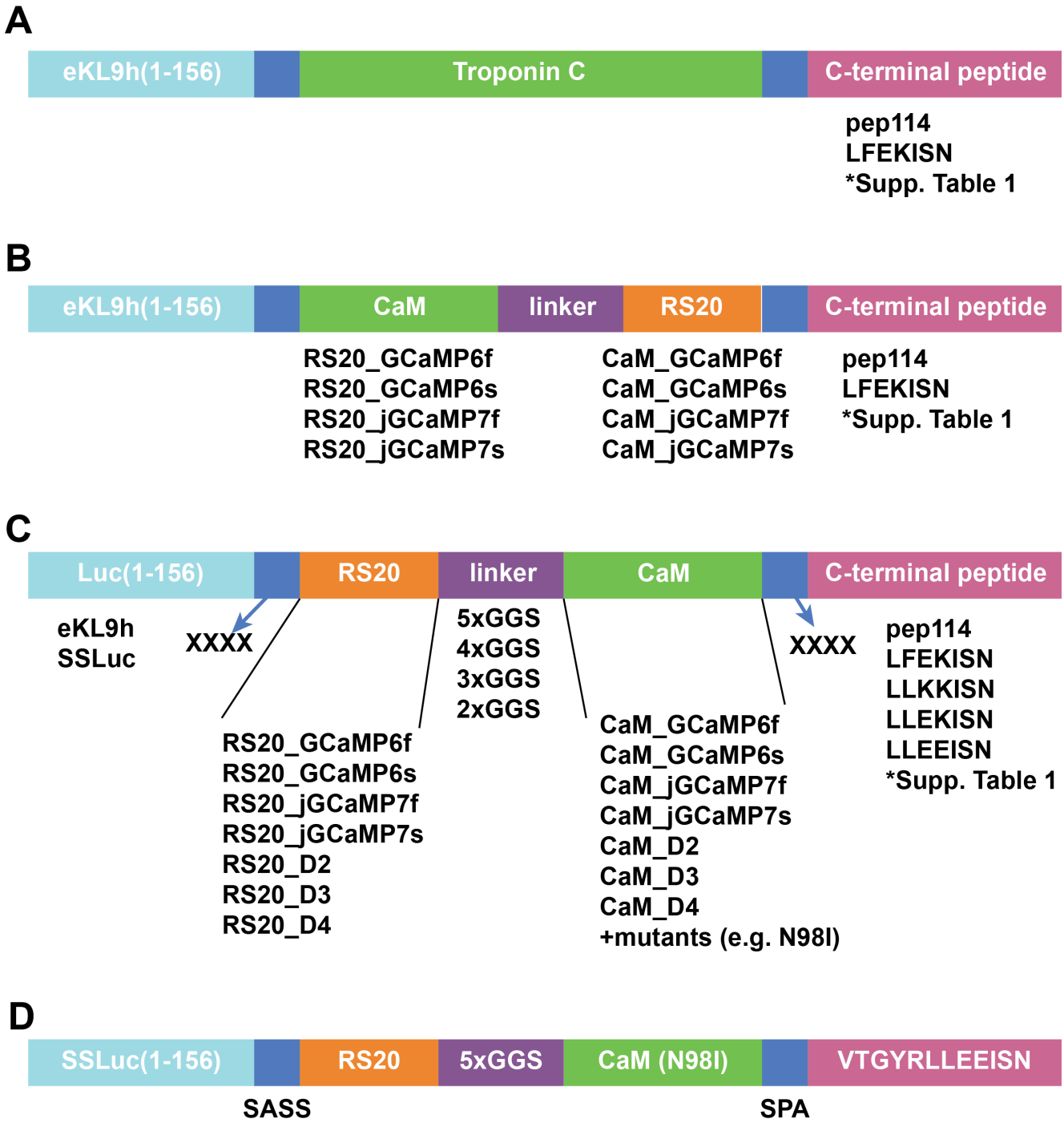


**Supplementary Figure 4.** BL GECI architectures investigated in this work. (A) Insertions of Troponin C domains produced working indicators with low contrast. (B) A calmodulin-linker-RS20 insertion into the luciferase was also functional but had low brightness regardless of the combination of components. (C) An RS20-linker-calmodulin insertion into the luciferase generated the highest brightness and contrast with tunable $Ca^{2+}$ affinity, ultimately leading us to the final CaBLAM design (D).

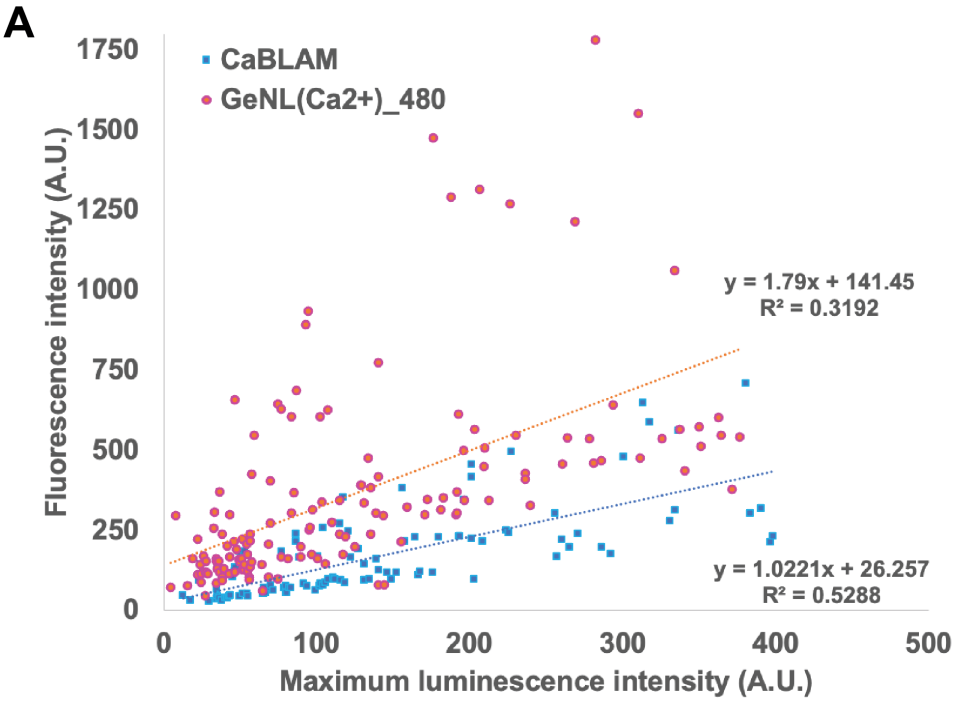


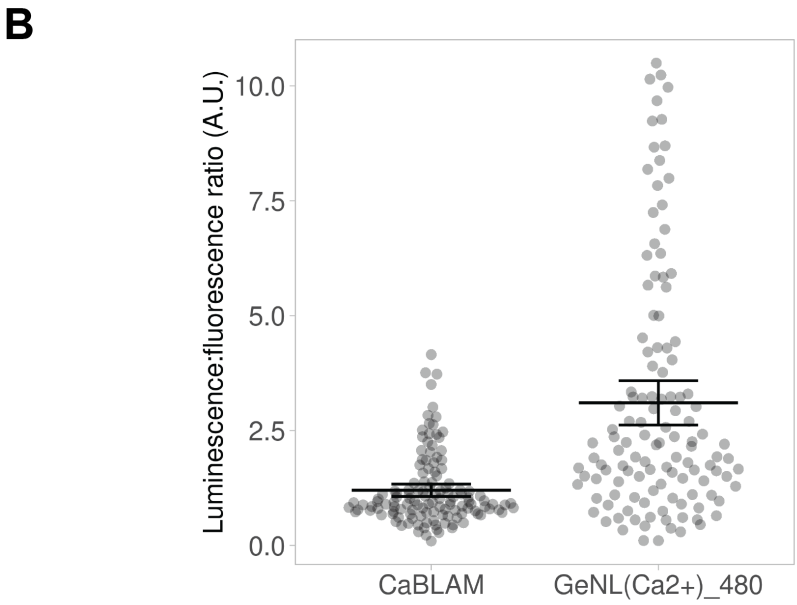


**Supplementary Figure 5.** Maximal brightness comparison of CaBLAM and GeNL($Ca^{2+}$)_480. (A) We observed a poor linear correlation between fluorescence intensity and maximal bioluminescence emission in cells expressing the lowest levels of each sensor, leading to a broad spread in fluorescence:bioluminescence ratios per cell (B). However, these data strongly suggest that CaBLAM is ~40% as bright as GeNL($Ca^{2+}$)_480 when both are $Ca^{2+}$-saturated.

**Other Supplementary Information**

**Supp Movie 1** — BL imaging of CaBLAM-expressing HeLa cells stimulated with l-histamine.

**Supp Movie 2** — BL imaging of CaBLAM-expressing rat hippocampal neurons with electrical stimulation

**Supp Data File 1** — peptide sequences of SSLuc, related OLucs, and intermediates, CaBLAM

**Supp Data File 2** — primer list

**References**


1. Shen Y, Nasu Y, Shkolnikov I, Kim A, Campbell RE. Engineering genetically encoded fluorescent indicators for imaging of neuronal activity: progress and prospects. Neurosci Res. 2020;152:3–14. PMID: 31991206

2. Lin MZ, Schnitzer MJ. Genetically encoded indicators of neuronal activity. Nat Neurosci. 2016;19(9):1142–1153. PMCID: PMC5557009

3. Hires SA, Tian L, Looger LL. Reporting neural activity with genetically encoded calcium indicators. Brain Cell Biol. 2008;36(1–4):69. PMCID: PMC2755531

4. Dong C, Zheng Y, Long-Iyer K, Wright EC, Li Y, Tian L. Fluorescence Imaging of Neural Activity, Neurochemical Dynamics, and Drug-Specific Receptor Conformation with Genetically Encoded Sensors. Annu Rev Neurosci. 2022;45(1):273–294. PMCID: PMC9940643

5. Zhang Y, Rózsa M, Liang Y, Bushey D, Wei Z, Zheng J, Reep D, Broussard GJ, Tsang A, Tsegaye G, Narayan S, Obara CJ, Lim JX, Patel R, Zhang R, Ahrens MB, Turner GC, Wang SSH, Korff WL, Schreiter ER, Svoboda K, Hasseman JP, Kolb I, Looger LL. Fast and sensitive GCaMP calcium indicators for imaging neural populations. Nature. 2023;615(7954):884–891. PMCID: PMC10060165

6. Li J, Shang Z, Chen JH, Gu W, Yao L, Yang X, Sun X, Wang L, Wang T, Liu S, Li J, Hou T, Xing D, Gill DL, Li J, Wang SQ, Hou L, Zhou Y, Tang AH, Zhang X, Wang Y. Engineering of NEMO as calcium indicators with large dynamics and high sensitivity. Nat Methods. 2023;1–7. PMID: 37081094

7. Doronin DA, Barykina NV, Subach OM, Sotskov VP, Plusnin VV, Ivleva OA, Isaakova EA, Varizhuk AM, Pozmogova GE, Malyshev AY, Smirnov IV, Piatkevich KD, Anokhin KV, Enikolopov GN, Subach FV. Genetically encoded calcium indicator with NTnC-like design and enhanced fluorescence contrast and kinetics. Bmc Biotechnol. 2018;18(1):10. PMID: 29439686

8. Dana H, Mohar B, Sun Y, Narayan S, Gordus A, Hasseman JP, Tsegaye G, Holt GT, Hu A, Walpita D, Patel R, Macklin JJ, Bargmann CI, Ahrens MB, Schreiter ER, Jayaraman V, Looger LL, Svoboda K, Kim DS. Sensitive red protein calcium indicators for imaging neural activity. eLife. 2016 Mar 24;5:413.

9. Qian Y, Cosio DMO, Piatkevich KD, Aufmkolk S, Su WC, Celiker OT, Schohl A, Murdock MH, Aggarwal A, Chang YF, Wiseman PW, Ruthazer ES, Boyden ES, Campbell RE. Improved genetically encoded near-infrared fluorescent calcium ion indicators for in vivo imaging. PLoS Biol. 2020;18(11):e3000965. PMCID: PMC7723245

10. Shimomura O, Johnson FH, SAIGA Y. Extraction, purification and properties of aequorin, a bioluminescent protein from the luminous hydromedusan, Aequorea. Journal of cellular and comparative physiology. 1962 Jun;59:223–239.

11. Musicki B, Kishi Y, Shimomura O. Structure of the functional part of photoprotein aequorin. Journal of the Chemical Society, Chemical Communications. 1986;(21):1566.

12. Naumann EA, Kampff AR, Prober DA, Schier AF, Engert F. Monitoring neural activity with bioluminescence during natural behavior. Nature Neuroscience. 2010 Apr;13(4):513–520.

13. Qian Y, Rancic V, Wu J, Ballanyi K, Campbell RE. A Bioluminescent Ca2+ Indicator Based on a Topological Variant of GCaMP6s. ChemBioChem. 2019;20(4):516–520. PMID: 29934970

14. Farhana I, Hossain MN, Suzuki K, Matsuda T, Nagai T. Genetically Encoded Fluorescence/Bioluminescence Bimodal Indicators for Ca 2+ Imaging. Acs Sensors. 2019;4(7):1825–1834. PMID: 31276380

15. Yang J, Cumberbatch D, Centanni S, Shi SQ, Winder D, Webb D, Johnson CH. Coupling optogenetic stimulation with NanoLuc-based luminescence (BRET) Ca(++) sensing. Nature communications. 2016 Oct 27;7:13268.

16. Saito K, Chang YF, Horikawa K, Hatsugai N, Higuchi Y, Hashida M, Yoshida Y, Matsuda T, Arai Y, Nagai T. Luminescent proteins for high-speed single-cell and whole-body imaging. Nature Communications. 2012 Dec 11;3(1):1262. PMID: 23232392

17. Suzuki K, Kimura T, Shinoda H, Bai G, Daniels MJ, Arai Y, Nakano M, Nagai T. Five colour variants of bright luminescent protein for real-time multicolour bioimaging. Nature Communications. 2016 Dec 7;7(1):1–10. PMID: 27966527

18. Oh Y, Park Y, Cho JH, Wu H, Paulk NK, Liu LX, Kim N, Kay MA, Wu JC, Lin MZ. An orange calcium-modulated bioluminescent indicator for non-invasive activity imaging. Nat Chem Biol. 2019;15(5):433–436. PMID: 30936501

19. Shimomura O, Masugi T, Johnson FH, Haneda Y. Properties and reaction mechanism of the bioluminescence system of the deep-sea shrimp Oplophorus gracilorostris. Biochemistry. 1978 Mar 21;17(6):994–998.

20. Inouye S, Watanabe K, Nakamura H, Shimomura O. Secretional luciferase of the luminous shrimp Oplophorus gracilirostris: cDNA cloning of a novel imidazopyrazinone luciferase. FEBS LETTERS. 2000 Sep;481(1):19–25. PMID: 10984608

21. Inouye S, Sasaki S. Overexpression, purification and characterization of the catalytic component of Oplophorus luciferase in the deep-sea shrimp, Oplophorus gracilirostris. Protein Expression and Purification. 2007 Dec;56(2):261–268.

22. Inouye S, Sato J ichi, Sahara-Miura Y, Yoshida S, Hosoya T. Luminescence enhancement of the catalytic 19kDa protein (KAZ) of Oplophorus luciferase by three amino acid substitutions. Biochemical and Biophysical Research Communications. 2014 Feb 28;445(1):157–162.

23. Shaner NC, Lambert GG, Chammas A, Ni Y, Cranfill PJ, Baird MA, Sell BR, Allen JR, Day RN, Israelsson M, Davidson MW, Wang J. A bright monomeric green fluorescent protein derived from Branchiostoma lanceolatum. Nature Methods. 2013 May;10(5):407–409. PMCID: PMC3811051

24. Hall MP, Unch J, Binkowski BF, Valley MP, Butler BL, Wood MG, Otto P, Zimmerman K, Vidugiris G, Machleidt T, Robers MB, Benink HA, Eggers CT, Slater MR, Meisenheimer PL, Klaubert DH, Fan F, Encell LP, Wood KV. Engineered Luciferase Reporter from a Deep Sea Shrimp Utilizing a Novel Imidazopyrazinone Substrate. ACS Chemical Biology. 2012 Nov 16;7(11):1848–1857.

25. Dixon AS, Schwinn MK, Hall MP, Zimmerman K, Otto P, Lubben TH, Butler BL, Binkowski BF, Machleidt T, Kirkland TA, Wood MG, Eggers CT, Encell LP, Wood KV. NanoLuc Complementation Reporter Optimized for Accurate Measurement of Protein Interactions in Cells. ACS Chemical Biology. 2015 Dec 10;11(2):400–408.

26. Förster T. Zwischenmolekulare Energiewanderung Und Fluoreszenz. Annalen Der Physik. 1948;2(1–2):55–75.

27. Takai A, Nakano M, Saito K, Haruno R, Watanabe TM, Ohyanagi T, Jin T, Okada Y, Nagai T. Expanded palette of Nano-lanterns for real-time multicolor luminescence imaging. Proceedings of the National Academy of Sciences. 2015 Apr 7;112(14):4352–4356. PMID: 25831507

28. Dana H, Sun Y, Mohar B, Hulse BK, Kerlin AM, Hasseman JP, Tsegaye G, Tsang A, Wong A, Patel R, Macklin JJ, Chen Y, Konnerth A, Jayaraman V, Looger LL, Schreiter ER, Svoboda K, Kim DS. High-performance calcium sensors for imaging activity in neuronal populations and microcompartments. Nat Methods. 2019;16(7):649–657. PMID: 31209382

29. Chen TW, Wardill TJ, Sun Y, Pulver SR, Renninger SL, Baohan A, Schreiter ER, Kerr RA, Orger MB, Jayaraman V, Looger LL, Svoboda K, Kim DS. Ultrasensitive fluorescent proteins for imaging neuronal activity. Nature. 2013 Jul 18;499(7458):295–300.

30. Mank M, Reiff DF, Heim N, Friedrich MW, Borst A, Griesbeck O. A FRET-Based Calcium Biosensor with Fast Signal Kinetics and High Fluorescence Change. Biophysical Journal. 2006 Mar 1;90(5):1790–1796.

31. Palmer AE, Giacomello M, Kortemme T, Hires SA, Lev-Ram V, Baker D, Tsien RY. Ca2+ Indicators Based on Computationally Redesigned Calmodulin-Peptide Pairs. Chemistry & Biology [Internet]. 2006 May;13(5):521–530.

32. Jensen HH, Brohus M, Nyegaard M, Overgaard MT. Human Calmodulin Mutations. Front Mol Neurosci. 2018;11:396. PMCID: PMC6243062

33. Maravall M, Mainen ZF, Sabatini BL, Svoboda K. Estimating Intracellular Calcium Concentrations and Buffering without Wavelength Ratioing. Biophys J. 2000;78(5):2655–2667. PMCID: PMC1300854

34. Lovell S, Mehzabeen N, Battaile KP, Wood MG, Unch J, Encell LP, Wood KV. 2.20A Resolution Structure of NanoLuc Luciferase with Bound Substrate Analog 3-methoxy-furimazine. 2022;

35. Sauvé R, Diarra A, Chahine M, Simoneau C, Morier N, Roy G. Ca2+ oscillations induced by histamine H1 receptor stimulation in HeLa cells: Fura-2 and patch clamp analysis. Cell Calcium. 1991;12(2–3):165–176. PMID: 2059991

36. Zenchak JR, Palmateer B, Dorka N, Brown TM, Wagner LM, Medendorp WE, Petersen ED, Prakash M, Hochgeschwender U. Bioluminescence-driven optogenetic activation of transplanted neural precursor cells improves motor deficits in a Parkinson's disease mouse model. Journal of Neuroscience Research. 2018 Mar 25;90(5):955.

37. Crespo EL, Prakash M, Bjorefeldt A, Medendorp WE, Shaner NC, Lipscombe D, Moore CI, Hochgeschwender U. Bioluminescent optogenetic (BL-OG) activation of neurons during mouse postnatal brain development. Star Protoc. 2021;2(3):100667. PMCID: PMC8273415

38. Crespo EL, Bjorefeldt A, Prakash M, Hochgeschwender U. Bioluminescent Optogenetics 2.0: Harnessing Bioluminescence to Activate Photosensory Proteins In Vitro and In Vivo. J Vis Exp. 2021;(174). PMID: 34424228

39. English AW, Berglund K, Carrasco D, Goebel K, Gross RE, Isaacson R, Mistretta OC, Wynans C. Bioluminescent Optogenetics: A Novel Experimental Therapy to Promote Axon Regeneration after Peripheral Nerve Injury. Int J Mol Sci. 2021;22(13):7217. PMID: 34281270

40. Sureda-Vives M, Sarkisyan KS. Bioluminescence-Driven Optogenetics. Life. 2020;10(12):318. PMID: 33260589

41. Tung JK, Gutekunst CA, Gross RE. Inhibitory luminopsins: genetically-encoded bioluminescent opsins for versatile, scalable, and hardware-independent optogenetic inhibition. Scientific Reports. 2015 Sep 24;5:14366.

42. Petersen ED, Sharkey ED, Pal A, Shafau LO, Zenchak-Petersen J, Peña AJ, Aggarwal A, Prakash M, Hochgeschwender U. Restoring Function After Severe Spinal Cord Injury Through BioLuminescent-OptoGenetics. Front Neurol. 2022;12:792643. PMCID: PMC8811305

43. Petersen ED, Crespo EL, Lambert GG, Zanca AT, Orcutt R, Hochgeschwender U, Shaner NC, Gilad AA. Bioluminescent Genetically Encoded Glutamate Indicator for Molecular Imaging of Neuronal Activity. Biorxiv. 2021;2021.06.16.448690.

44. Gibson DG, Young L, Chuang RY, Venter JC, Hutchison CA, Smith HO. Enzymatic assembly of DNA molecules up to several hundred kilobases. Nature Publishing Group. 2009 May;6(5):343–345.

45. Lambert GG, Depernet H, Gotthard G, Schultz DT, Navizet I, Lambert T, Adams SR, Torreblanca-Zanca A, Chu M, Bindels DS, Levesque V, Moffatt JN, Salih A, Royant A, Shaner NC. Aequorea's secrets revealed: New fluorescent proteins with unique properties for bioimaging and biosensing. Plos Biol. 2020;18(11):e3000936. PMCID: PMC7660908

46. Boassa D, Berlanga ML, Yang MA, Terada M, Hu J, Bushong EA, Hwang M, Masliah E, George JM, Ellisman MH. Mapping the Subcellular Distribution of α-Synuclein in Neurons using Genetically Encoded Probes for Correlated Light and Electron Microscopy: Implications for Parkinson's Disease Pathogenesis. J Neurosci. 2013;33(6):2605–2615. PMCID: PMC3711410

47. Berglund K, Clissold K, Li HE, Wen L, Park SY, Gleixner J, Klein ME, Lu D, Barter JW, Rossi MA, Augustine GJ, Yin HH, Hochgeschwender U. Luminopsins integrate opto- and chemogenetics by using physical and biological light sources for opsin activation. Proceedings of the National Academy of Sciences of the United States of America. 2016 Jan 19;113(3):E358-67.

48. Wardill TJ, Chen TW, Schreiter ER, Hasseman JP, Tsegaye G, Fosque BF, Behnam R, Shields BC, Ramirez M, Kimmel BE, Kerr RA, Jayaraman V, Looger LL, Svoboda K, Kim DS. A neuron-based screening platform for optimizing genetically-encoded calcium indicators. Plos One. 2013;8(10):e77728. PMCID: PMC3796516

49. Pachitariu M, Stringer C. Cellpose 2.0: how to train your own model. Nat Methods. 2022;19(12):1634–1641. PMCID: PMC9718665

50. Nagai T, Ibata K, Park ES, Kubota M, Mikoshiba K, Miyawaki A. A variant of yellow fluorescent protein with fast and efficient maturation for cell-biological applications. Nature Biotechnology. 2002 Jan 1;20(1):87–90.

51. Loening AM. Consensus guided mutagenesis of Renilla luciferase yields enhanced stability and light output. Protein Engineering Design and Selection. 2006 Jul 20;19(9):391–400.

52. Tomabechi Y, Hosoya T, Ehara H, Sekine S ichi, Shirouzu M, Inouye S. Crystal structure of nanoKAZ: The mutated 19 kDa component of Oplophorus luciferase catalyzing the bioluminescent reaction with coelenterazine. Biochemical and Biophysical Research Communications. 2016 Jan 29;470(1):88–93.

53. Mo X lei, Qi Q, Ivanov AA, Niu Q, Luo Y, Havel J, Goetze R, Bell S, Moreno CS, Cooper LAD, Johns MA, Khuri FR, Du Y, Fu H. AKT1, LKB1, and YAP1 revealed as MYC interactors with NanoLuc-based protein-fragment complementation assay. Mol Pharmacol. 2017;91(4):mol.116.107623. PMCID: PMC5363710

54. Verhoef LGGC, Mattioli M, Ricci F, Li YC, Wade M. Multiplex detection of protein–protein interactions using a next generation luciferase reporter. Biochim Biophys Acta (BBA) - Mol Cell Res. 2016;1863(2):284–292. PMID: 26646257

55. Ni Y, Arts R, Merkx M. Ratiometric Bioluminescent Sensor Proteins Based on Intramolecular Split Luciferase Complementation. ACS Sens. 2019;4(1):20–25. PMCID: PMC6350203

56. Leaver-Fay A, Tyka M, Lewis SM, Lange OF, Thompson J, Jacak R, Kaufman K, Renfrew PD, Smith CA, Sheffler W, Davis IW, Cooper S, Treuille A, Mandell DJ, Richter F, Ban YEA, Fleishman SJ, Corn JE, Kim DE, Lyskov S, Berrondo M, Mentzer S, Popović Z, Havranek JJ, Karanicolas J, Das R, Meiler J, Kortemme T, Gray JJ, Kuhlman B, Baker D, Bradley P. ROSETTA3: an object-oriented software suite for the simulation and design of macromolecules. Methods in Enzymology. 2011;487:545–574.

57. Inouye S, Sato J ichi, Sahara-Miura Y, Tomabechi Y, Sumida Y, Sekine S ichi, Shirouzu M, Hosoya T. Reverse mutants of the catalytic 19 kDa mutant protein (nanoKAZ/nanoLuc) from Oplophorus luciferase with coelenterazine as preferred substrate. PLoS ONE. 2022;17(9):e0272992. PMCID: PMC9491549

58. Dijkema FM, Nordentoft MK, Didriksen AK, Corneliussen AS, Willemoës M, Winther JR. Flash properties of Gaussia luciferase are the result of covalent inhibition after a limited number of cycles. Protein Sci. 2021;30(3):638–649. PMID: 33426745

59. Chou WC, Liao KW, Lo YC, Jiang SY, Yeh MY, Roffler SR. Expression of chimeric monomer and dimer proteins on the plasma membrane of mammalian cells. Biotechnology and Bioengineering. 1999 Oct 20;65(2):160–169.

60. Provost E, Rhee J, Leach SD. Viral 2A peptides allow expression of multiple proteins from a single ORF in transgenic zebrafish embryos. genesis. 2007;45(10):625–629.

61. Costantini LM, Fossati M, Francolini M, Snapp EL. Assessing the Tendency of Fluorescent Proteins to Oligomerize Under Physiologic Conditions. Traffic. 2012 Feb 20;13(5):643–649.